

Quantum control of photoelectron circular dichroism

R. Esteban Goetz,¹ Christiane P. Koch,² and Loren Greenman^{1,*}

¹*Department of Physics, Kansas State University,
116 Cardwell Hall, 1228 N. 17th St. Manhattan, KS 66506-2601*

²*Theoretische Physik, Universität Kassel, Heinrich-Plett-Str. 40, D-34132 Kassel, Germany*

(Dated: December 18, 2018)

We demonstrate coherent control over the photoelectron circular dichroism in randomly oriented chiral molecules, based on quantum interference between multiple photoionization pathways. To significantly enhance the chiral signature, we use a finite manifold of indistinguishable (1+1') REMPI pathways interfering at a common photoelectron energy but probing different intermediate states. We show that this coherent control mechanism maximizes the number of molecular states that constructively contribute to the dichroism at an optimal photoelectron energy and thus outperforms other schemes, including interference between opposite-parity pathways driven by bichromatic ($\omega, 2\omega$) fields as well as sequential pump-probe ionization.

Chiral molecules are non-superimposable mirror images of each other, referred to as enantiomers. Recent advances in measuring enantiomer-sensitive observables in gas phase table-top experiments [1–4] have brought chiral molecules into the spotlight of current AMO research. One of these observables is photoelectron circular dichroism (PECD), i.e., the differential photoelectron angular distribution obtained by ionizing randomly oriented molecules with left circularly and right circularly polarized light [1, 5–9]. PECD is a purely electric dipole effect, yielding much stronger signals than traditional absorption circular dichroism (CD), which involves also the magnetic dipole of the probed transition. It can be quantified by the odd-moment coefficients in the expansion of the photoelectron angular distribution into Legendre polynomials. The simplest explanation for PECD is provided by perturbation theory for one-photon ionization [10]: It is the small difference in magnitude between dipole matrix elements with opposite sign m quantum number, occurring only for chiral molecules, that results in a net effect when averaging over all molecular orientations. More intuitively, two non-parallel vectors are needed to provide an orientation with which to probe the handedness of the molecular scaffold and create a pseudo-scalar observable. While in traditional CD these are the electric and magnetic dipole moment, the photoelectron momentum provides the second vector in PECD. This picture connects PECD with the general framework for electric-dipole-based chiral observables [11]. Perturbation theory can also explain the PECD observed in resonantly enhanced multi-photon ionization (REMPI) [1], in terms of the electronically excited intermediate state of the REMPI process [12]. Dependence of the chiral signal on excitation wavelength is then understood in terms of probing different intermediate states [13]. Whether PECD is amenable to coherent control by suitably shaping the ionizing pulses is an open question [14].

Here, we address this question by making use of opti-

mal control theory and show that, for a chiral methane derivative, CHBrClF, quantum interference between distinct two-photon ionization pathways significantly enhances PECD. To this end, we combine a many-body description of the electron dynamics, scattering theory to efficiently describe the photoelectron continuum [5–7], and second-order time-dependent perturbation theory with an optimization technique [10]. We use this approach to maximize the PECD for CHBrClF while fully accounting for the chiral nature of the potential experienced by the photoelectron. We use CHBrClF as one of the simplest chiral molecules that has featured prominently in recent experiments [3] but expect our findings to be relevant for larger molecules as well.

We first detail our methodology to calculate the photoelectron spectrum and PECD. Keeping the nuclei fixed and neglecting relativistic effects, the Schrödinger equation for the many electron system reads

$$i \frac{\partial}{\partial t} |\Psi^N(t)\rangle = [\hat{H}_0 + \hat{H}_1 - \mathcal{E}(t) \cdot \hat{\mathbf{r}}] |\Psi^N(t)\rangle, \quad (1)$$

where \hat{H}_0 and \hat{H}_1 refer to the mean-field Fock operator and the residual Coulomb interaction, respectively. Accounting for one-particle one-hole excitations only, the many-body wave function is described by the manifold [19]

$$|\Psi^N(t)\rangle = \alpha_0(t) e^{-i\varepsilon_0 t} |\Phi_0\rangle + \sum_{i,a} \alpha_i^a(t) e^{-i\varepsilon_i^a t} |\Phi_i^a\rangle \quad (2) \\ + \sum_i \int d\mathbf{k} \alpha_i^{\mathbf{k}}(t) e^{-i\varepsilon_i^{\mathbf{k}} t} |\Phi_i^{\mathbf{k}}\rangle,$$

where $\alpha_0(t)$, $\alpha_i^a(t)$ and $\alpha_i^{\mathbf{k}}(t)$ are time-dependent coefficients, and $|\Phi_0\rangle$ refers to the Hartree-Fock ground state. $|\Phi_i^a\rangle = \hat{\mathbf{c}}_a^\dagger \hat{\mathbf{c}}_i |\Phi_0\rangle$ and $|\Phi_i^{\mathbf{k}}\rangle$ describe one-particle one-hole excitations from an initially occupied orbital i to a bound unoccupied orbital a or a continuum state with energy $|\mathbf{k}|^2/2$. To model an ensemble of randomly oriented molecules, we average over all Euler angles $\gamma_{\mathcal{R}} = (\alpha, \beta, \gamma)$, see supplemental material [20] for detailed description, which also contains Refs. [2–12]. The

* lgreenman@phys.ksu.edu

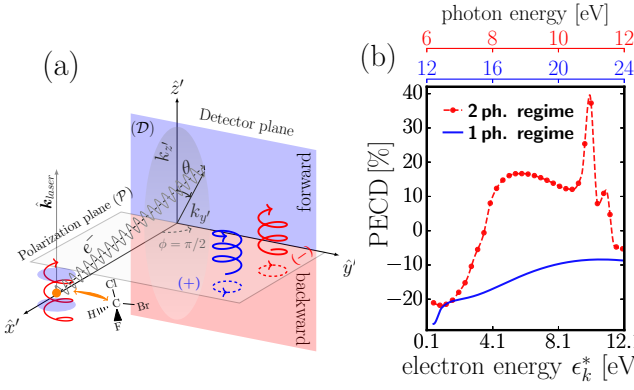


FIG. 1. (a) A randomly oriented ensemble of CHBrClF molecules (orange ball) is ionized with left (+) or right (-) circularly polarized light, and the emitted electron is measured in the (z', y') -plane. The polarization plane (\mathcal{P}) defines the (x', y') -plane and the vector z' normal to \mathcal{P} is given by the laser propagation direction. (b) Maximum PECD over all angles as a function of the photoelectron energy after ionization by a Gaussian pulse with central frequency ω denoted in terms of photon energy. The photon order is determined using the anisotropy parameters in Eq. (8).

orientation-averaged photoelectron momentum distribution is obtained upon integration over $\gamma_{\mathcal{R}}$ and incoherent summation over the initially occupied contributing orbitals i in the Hartree-Fock ground state,

$$\frac{d^2\sigma}{d\epsilon_k d\Omega_{\mathbf{k}'}} = \sum_{i \in \text{occ}} \int |\alpha_i^{\mathbf{k}'}(t; \gamma_{\mathcal{R}})|^2 d^3\gamma_{\mathcal{R}}, \quad (3)$$

for $t \rightarrow \infty$ and with \mathbf{k}' denoting the momentum measured in the laboratory frame, defined by the propagation direction of the light beam along z' , as indicated in Fig. 1(a). The photoionization process is captured by the coefficients $\alpha_i^{\mathbf{k}'}(t; \gamma_{\mathcal{R}})$. It requires an accurate description of the scattering portion of the wave function, which presents a formidable computational challenge for a many-electron system with no symmetry. To reduce the computational cost, we resort to solving Eq. (1) perturbatively. A second-order treatment allows us to manipulate quantum interferences between conventional opposite-parity, as well as same-parity (two-photon) pathways. These interferences can be exploited to control the differential and integral cross section in systems with no inversion center of symmetry [28, 29]. Restricting the maximum field amplitude and the ionization yield to ensure the validity of the perturbation approximation, Eq. (3) simplifies to

$$\frac{d^2\sigma}{d\epsilon_k d\Omega_{\mathbf{k}'}} \approx \int |\alpha_{i_0}^{\mathbf{k}'(1)}(t; \gamma_{\mathcal{R}}) + \alpha_{i_0}^{\mathbf{k}'(2)}(t; \gamma_{\mathcal{R}})|^2 d^3\gamma_{\mathcal{R}}, \quad (4)$$

for $t \rightarrow \infty$ and with $\alpha_{i_0}^{\mathbf{k}'(1,2)}(t; \gamma_{\mathcal{R}})$, the first, resp. second, order correction [20]. Second-order terms account for two-photon ionization pathways, from i_0 to \mathbf{k}' via different unoccupied orbitals a .

We restrict the electron dynamics to be influenced by the mean-field molecular electrostatic potential and time-dependent field only. The orbitals participating during the photoionization are described by the manifold of the HOMO (labeled i_0 , with ionization potential ω_0) and unoccupied orbitals defined by the eigenfunctions of the field-free Fock operator together with the scattering states defined by the excitation $|\Phi_{i_0}^{\mathbf{k}'}\rangle$. The Hartree-Fock orbitals were obtained using the MOLPRO [11, 12] program package with the aug-cc-pVDZ basis set [30]. The scattering portion $\varphi_{\mathbf{k}}^-(\mathbf{r})$ of the total wave function is an eigenfunction of the scattering problem,

$$\left[-\frac{\nabla^2}{2} - \frac{1}{r} + \hat{\mathbf{V}} - \frac{k^2}{2}\right] \varphi_{\mathbf{k}}^-(\mathbf{r}) = 0, \quad (5)$$

where $\hat{\mathbf{V}}(\mathbf{r})$ is the short-range part of the electron-ion interaction. Equation (5) is solved using a locally modified version of the ePolyScat program package [5–7], see the supplemental material [20] for more detail. PECD is calculated by expanding Eq. (4) into Legendre polynomials P_ℓ^m ,

$$\frac{d^2\sigma(\pm)}{d\epsilon_k d\Omega_{\mathbf{k}'}} = \sum_{\ell, m} \beta_{\ell, m}^{(\pm)}(\epsilon_k) P_\ell^m(\cos\theta') e^{im\varphi'}, \quad (6)$$

where \pm distinguishes the momentum distribution obtained with left (+) and right (-) circularly polarized light. The anisotropy parameters $\beta_{\ell, m}^{(\pm)}(\epsilon_k)$ are decomposed into contributions from the one- and two-photon ionization pathways and their interference,

$$\beta_{\ell, m}^{(\pm)}(\epsilon_k) = \beta_{\ell, m}^{(\pm)1ph}(\epsilon_k) + \beta_{\ell, m}^{(\pm)2ph}(\epsilon_k) + \beta_{\ell, m}^{(\pm)int}(\epsilon_k). \quad (7)$$

PECD is the non-vanishing component that remains after subtracting Eq. (6) obtained with left and right circularly polarized light [1, 5–9] and reads [20], for $\phi = \pi/2$,

$$\begin{aligned} \text{PECD}(\epsilon_k, \theta, \phi = \pi/2) &= 2 \sum_{n, k} \beta_{2k+1, 0}^{(+nph)}(\epsilon_k) P_{2k+1}^0(\cos\theta) \\ &+ 6 \text{Im}[\beta_{2, 1}^{(+int)}(\epsilon_k)] \sin(2\theta). \end{aligned} \quad (8)$$

Anisotropy parameters and PECD are expressed in percentage of the peak photoelectron intensity. The driving electric field is parametrized,

$$\epsilon(t) = \sum_{j=1}^2 \epsilon_j e^{-(t-\tau_j)^2/2\sigma_j^2} \cos(\omega_j(t-\tau_j) + \phi_j), \quad (9)$$

with ϵ_j , ω_j , ϕ_j the amplitude, frequency, and carrier envelope phase of the j th pulse with full width at half maximum $\text{FWHM} = 2\sqrt{2 \ln 2} \sigma_j$ and time delay τ_j , which are optimized following Ref. [10]. To ensure the validity of the perturbation approximation, we constrain the maximal peak intensity to values not exceeding $1.0 \times 10^{11} \text{ W/cm}^2$, which was found to be an appropriate upper limit in bichromatic photoionization studies [31].

We first resolve the PECD as a function of the photon energy using a 25 fs (FWHM) monochromatic laser field

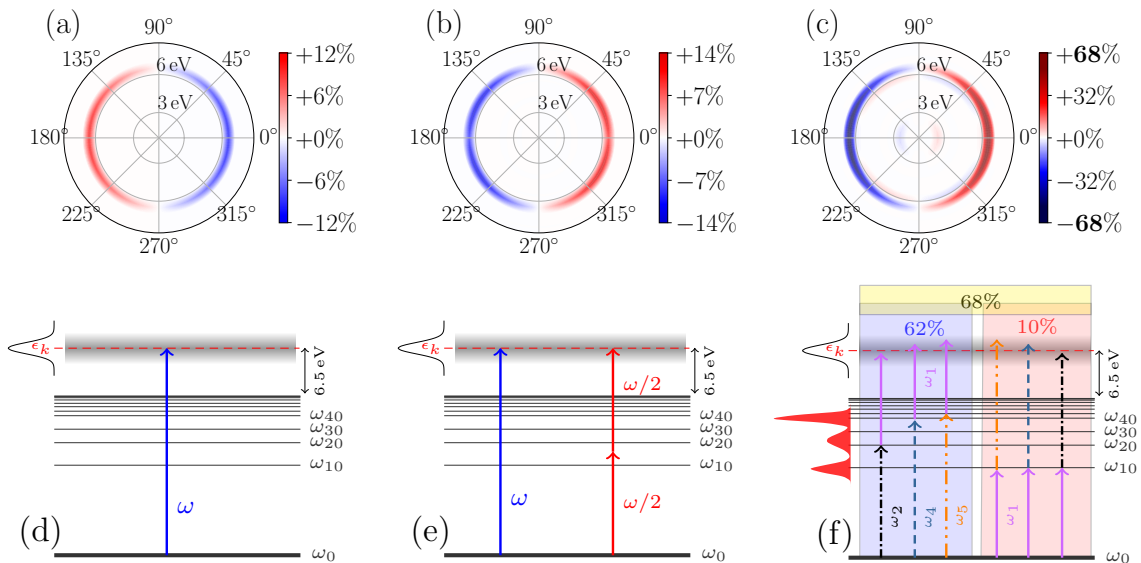


FIG. 2. (a-c): Angularly resolved PECD obtained with (a) a monochromatic reference field driving one-photon ionization, (b) an optimized bichromatic ($\omega, 2\omega$) pulse, and (c) making use of interference in even-parity two-photon pathways. (d-f): Corresponding ionization schemes. The control mechanism for two-photon pathway interference (f) is based on probing different intermediate states that interfere constructively at a common continuum photoelectron energy within the spectral bandwidth. Restricting the control mechanism to the pump-probe scenario with time-delayed pulses results in a PECD of 62%, resp. 10%, whereas pulses overlapping in time realize the maximum PECD of 68%.

(single frequency component in Eq. (9)) with peak intensity $I_0 = 5 \times 10^{10} \text{ W/cm}^2$. The resulting single- and two-photon PECD as a function of the photoelectron energy are shown in Fig. 1(b). Figure 2(a) shows the angularly resolved PECD for a photon energy of 18.4 eV. We now address the question whether the PECD can be enhanced by allowing for more ionization pathways including their interference to contribute.

The use of quantum interference between one- and two-photoionization pathways is a general, well-documented control mechanism [28, 29, 31, 32], and bichromatic pulses have been suggested to realize this scenario for atoms using linearly [32] and circularly [31] polarized light. Control of anisotropy after bichromatic ionization is also predicted for randomly oriented chiral molecules [33]. In this letter, we demonstrate, however, that interference between distinct two-photon ionization pathways results in a more efficient control mechanism to maximize PECD.

To this end, we first optimize driving fields constraining the frequency components to bichromatic ($\omega, 2\omega$) pulses. The PECD resulting from the optimized bichromatic ($\omega, 2\omega$) pulse reaches a maximum PECD of 20% at a photoelectron energy of 10 eV. This is comparable to asymmetries predicted for ($\omega, 2\omega$) bichromatic fields, linearly polarized in two mutually-orthogonal directions employing rotationally tailored laser pulses for control [33]. In a second step, we allow complete freedom for the photon energies of the driving field. With a maximal peak intensity of $3.5 \times 10^{10} \text{ W/cm}^2$ (for a total ionization yield of 6%), the fully optimized field is found to significantly

enhance the PECD to 68%. The corresponding photoelectron spectrum peaks at an energy of 6.5 eV.

PECD is known to strongly depend on the final continuum states. It is therefore important to disentangle the kinetic energy effects, i.e., contributions arising from the final continuum state –here with energy 6.5 eV and 10 eV – and those from different photoionization pathways leading to the same final state. We therefore compare the PECD obtained with a reference field driving one-photon ionization, the optimized bichromatic ($\omega, 2\omega$) and fully optimized pulses resulting in the same photoelectron kinetic energy.

The results for a photoelectron kinetic energy of 6.5 eV are shown in Fig. 2, whereas those for 10 eV are found in the supplemental material [20]. At a photoelectron energy of 6.5 eV, the PECD is enhanced from 12% using one-photon ionization to 14% using an interfering two-photon ionization pathway, i.e., bichromatic control, whereas a single two-photon ionization pathway that don't include interference reaches 16.2% PECD at 6.5 eV as shown in Fig. 1(b).

All of these are significantly smaller than 68% obtained for the fully optimized pulse where only two-photon pathways, but many more of them, cf. Fig. 2(f), interfere. This picture holds also at a photoelectron kinetic energy of 10 eV, where the maximum PECD for the reference field, optimized bichromatic ($\omega, 2\omega$) and fully-optimized pulses amounts to 8.5%, 20% and 64%, respectively [20].

The control mechanism for the fully optimized field of Fig. 2(f) is further analyzed in Fig. 3 with Fig. 3(a) showing the different anisotropy parameters for the fully

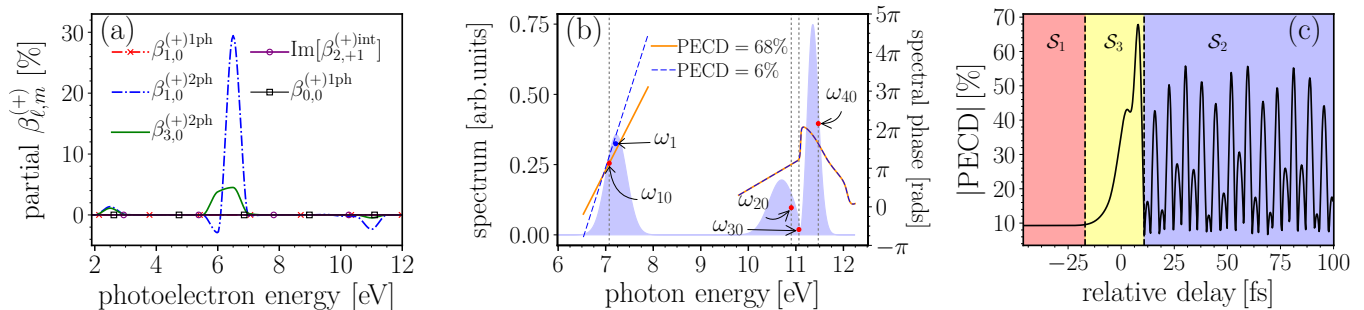


FIG. 3. Anisotropy parameters (a) for the fully optimized field as used in Fig. 2(c). Spectrum (blue) and spectral phase (solid orange line) of the fully optimized pulse are shown in (b). The frequencies ω_{j0} denote the transition energies between the HOMO and LUMO + $j - 1$ orbitals. Modifying the spectral phase (orange solid vs blue dashed lines) while keeping the spectrum unchanged dramatically alters the PECD. PECD as a function of the time delay (c) between the ω_1 -component and the higher frequency components of the optimized pulse shown in panel (b). In regions S_1 and S_2 , the subpulses are temporally separated (pump-probe scenario) with S_1 corresponding to ionization via the LUMO only (cf. right part of Fig. 2(f)) whereas in S_2 , ionization proceeds via a superposition of different excited states without the LUMO (cf. left part of Fig. 2(f)). In S_3 , pump and probe pulses overlap in time such that interference between all two-photon ionization pathways can be exploited.

optimized pulse. In contrast to the reference and optimized bichromatic ($\omega, 2\omega$) pulses, neither single-photon ionization nor interference between one- and two-photon pathways contribute for the fully optimized pulse. In fact, both $\beta_{1,0}^{(+1)ph}$ and $\beta_{2,+1}^{(+int)}$ vanish over the entire energy domain. Furthermore, the one-photon ionization pathway is completely suppressed, even for the symmetric part, since $\beta_{0,0}^{(+1)ph} = 0$. Instead, the remarkable enhancement of the PECD is indeed solely due to even-parity, i.e., two-photon ionization pathways because both $\beta_{1,0}^{(+2)ph}$ and $\beta_{3,0}^{(+2)ph}$ are non-zero.

Analyzing the spectrum of the fully optimized field, shown in Fig. 3(b), we identify the interference between different two-photon ionization pathways to give rise to the control observed in Fig. 2(c). The spectrum contains peaks at $\omega_1 = 7.24$ eV, $\omega_2 = 10.70$ eV, and $\omega_3 = 11.35$ eV and overlaps with transitions from the HOMO to the first unoccupied orbitals, namely, $\omega_{10} = 7.07$ eV, $\omega_{20} = 10.90$ eV, $\omega_{30} = 11.06$ eV and $\omega_{40} = 11.47$ eV, which need to be compared to the calculated ionization threshold of 11.88 eV. The two-photon ionization pathway $2 \times \omega_{10}$ promotes the photoelectron to 2.27 eV and explains the small peak at 2.39 eV in Fig. 3(a). Conversely, the pathways $2 \times \omega_2$, $\omega_2 + \omega_3$, $\omega_2 + \omega_4$, \dots , explain the small PECD at 11 eV. However, these pathways do not contribute much to PECD which is mainly due to the peak at 6.5 eV. The most important pathways leading to 6.5 eV, cf. Fig. 1(f), are $\omega_{20} + (\omega_{10} + \delta\omega_1)$ and similarly $(\omega_{10} + \delta\omega_1) + \omega_{20}$ with an offset of $\delta\omega_1 = 0.4$ eV as well as $\omega_{40} + (\omega_{10} - \delta\omega)$ with $\delta\omega = 0.12$ eV. The latter probes the LUMO+3, whereas the former two probe the LUMO+1 and LUMO. The required offsets are available within the spectral bandwidth. The pathways $\omega_{30} + \omega_{10}$ and $\omega_{10} + \omega_{30}$, probing the LUMO+2, are also compatible with the pulse spectrum; however, the frequency ω_{30} is suppressed, and removing the LUMO + 2 decreases the PECD by only 0.4%. In other words, the high frequency components of the op-

timized field correspond to photon energies which resonantly excite the first LUMO + j orbitals ($j = 1, 2, \dots$), while the peak centered at ω_1 can either excite the LUMO from the ground state or ionize the LUMO+ j population, cf. Fig. 2(f). Its bandwidth guarantees interference at a common photoelectron energy. Thus, the width and peak position at ω_1 are key for the constructive interference among a finite manifold of two-photon ionization pathways at a common final photoelectron energy to significantly enhance PECD. Constraining ω_1 to be exactly ω_{10} while reducing its spectral bandwidth results in a smaller PECD ($\approx 50\%$). Conversely, allowing ω_1 to be further blue-shifted with respect to ω_{10} while increasing the spectral bandwidth such that it still overlaps with ω_{10} results in a PECD of about 70% (not shown due to the large bandwidth of the field).

The coherent nature of the control mechanism is further confirmed by modifying the spectral phase of the optimized pulse while keeping the spectral amplitude unaffected, cf. dashed lines in Fig. 3(b). This corresponds to introducing a time delay between the high and low-frequency components of the pulse. Figure 3(c) shows the variation of the PECD, between 68% to 6%, as a function of this time delay. Positive (negative) delays correspond to the high-frequency components arriving before (after) the low-frequency components, as verified by inspecting the Wigner distribution function of the pulses. For negative time delays, highlighted in red in Figs. 2(f) and 3(c), only the LUMO is excited. PECD thus does not depend on the time delay and reflects the chiral signature of the LUMO only, which amounts to about 10%. For positive time delays, highlighted in blue in Figs. 2(f) and 3(c), the high-frequency components of the pulse prepare a superposition of higher excited states, such that the PECD depends on the time delay and contains the chiral fingerprints of the LUMO+ j ($j \geq 1$) with a maximum of 55%. These two scenarios correspond to pump-probe control [34, 35] where the pump pulse spectrum se-

lects the manifold of intermediate states that contribute. PECD can be pushed to 62% by further optimization of time-separated pump and probe pulses for positive delays. However, the maximal value of PECD, 68%, is obtained when pump and probe overlap, as highlighted in yellow in Figs. 2(f) and 2(c). This can be rationalized by exploiting interference of all the pathways, including the two-photon ionization through the LUMO, depicted in Fig. 2(f).

In conclusion, we have identified constructive interference in two-photon photoionization to significantly enhance PECD of randomly oriented CHBrClF molecules. Control is achieved via various $(1+1')$ REMPI pathways leading to a common final photoelectron state but probing different intermediate states. Separating pump and probe photons in time slightly reduces the number of pathways that may interfere and thus the PECD. In this excitation scheme based on interference of same-parity pathways, we find significantly larger PECD than can

be obtained with optimized bichromatic circularly polarized fields where opposite parity pathways are made to interfere constructively. It will be straightforward to extend this type of control to molecules other than CHBrClF, with only the central frequencies and spectral widths depending on the specific chiral molecule. Higher-order terms in the perturbation expansion, while requiring larger amplitudes, are likely to facilitate even more pathway interference and could also be used to drive photoionization with optical instead of XUV pulses. Whether an upper bound to PECD exists and what type of driving field would saturate it is yet unknown.

We would like to thank Thomas Baumert for helpful comments on the manuscript. The computing for this project was performed on the Beocat Research Cluster at Kansas State University, which is funded in part by NSF grants CNS-1006860, EPS-1006860, and EPS-0919443. CPK acknowledges financial support from the Deutsche Forschungsgemeinschaft (CRC 1319).

-
- [1] C. Lux, M. Wollenhaupt, T. Bolze, Q. Liang, J. Köhler, C. Sarpe, and T. Baumert, *Angew. Chem. Int. Ed.* **51**, 5001 (2012).
- [2] D. Patterson, M. Schnell, and J. M. Doyle, *Nature* **497**, 475 (2013).
- [3] M. Pitzer, M. Kunitski, A. S. Johnson, T. Jahnke, H. Sann, F. Sturm, L. P. H. Schmidt, H. Schmidt-Böcking, R. Dörner, J. Stohner, J. Kiedrowski, M. Reggelin, S. Marquardt, A. Schießer, R. Berger, and M. S. Schöffler, *Science* **341**, 1096 (2013).
- [4] P. Herwig, K. Zawatzky, M. Grieser, O. Heber, B. Jordon-Thaden, C. Krantz, O. Novotný, R. Repnow, V. Schurig, D. Schwalm, Z. Vager, A. Wolf, O. Trapp, and H. Kreckel, *Science* **342**, 1084 (2013).
- [5] N. Böwering, T. Lischke, B. Schmidtke, N. Müller, T. Khalil, and U. Heinzmann, *Phys. Rev. Lett.* **86**, 1187 (2001).
- [6] U. J. Meierhenrich, J.-J. Filippi, C. Meinert, J. H. Bredehöft, J.-i. Takahashi, L. Nahon, N. C. Jones, and S. V. Hoffmann, *Angew. Chem. Int. Ed.* **49**, 7799 (2010).
- [7] C. S. Lehmann, N. B. Ram, I. Powis, and M. H. M. Janssen, *J. Chem. Phys.* **139**, 234307 (2013).
- [8] A. Comby, S. Beaulieu, M. Boggio-Pasqua, D. Descamps, F. Légaré, L. Nahon, S. Petit, B. Pons, B. Fabre, Y. Mairesse, and V. Blanchet, *J. Phys. Chem. Lett.* **7**, 4514 (2016).
- [9] S. Beaulieu, A. Comby, A. Clergerie, J. Caillat, D. Descamps, N. Dudovich, B. Fabre, R. Généaux, F. Légaré, S. Petit, B. Pons, G. Porat, T. Ruchon, R. Taïeb, V. Blanchet, and Y. Mairesse, *Science* **358**, 1288 (2017).
- [10] B. Ritchie, *Phys. Rev. A* **13**, 1411 (1976).
- [11] A. F. Ordonez and O. Smirnova, arXiv:1802.06540 (2018).
- [12] R. E. Goetz, T. A. Isaev, B. Nikoobakht, R. Berger, and C. P. Koch, *J. Chem. Phys.* **146**, 024306 (2017).
- [13] A. Kastner, T. Ring, B. C. Krüger, G. B. Park, T. Schäfer, A. Senftleben, and T. Baumert, *J. Chem. Phys.* **147**, 013926 (2017).
- [14] M. Wollenhaupt, *New J. Phys.* **18**, 121001 (2016).
- [5] F. A. Gianturco, R. R. Lucchese, and N. Sanna, *J. Chem. Phys.* **100**, 6464 (1994).
- [6] A. P. P. Natalense and R. R. Lucchese, *J. Chem. Phys.* **111**, 5344 (1999).
- [7] L. Greenman, R. R. Lucchese, and C. W. McCurdy, *Phys. Rev. A* **96**, 052706 (2017).
- [10] R. E. Goetz, M. Merkel, A. Karamatskou, R. Santra, and C. P. Koch, *Phys. Rev. A* **94**, 023420 (2016).
- [19] T. Klamroth, *Phys. Rev. B* **68**, 245421 (2003).
- [20] Supplemental Material.
- [2] A. Szabo and N. S. Ostlund, *Modern quantum chemistry: introduction to advanced electronic structure theory* (Courier Corporation, 2012).
- [3] M. Baertschy, T. N. Rescigno, and C. W. McCurdy, *Phys. Rev. A* **64**, 022709 (2001).
- [4] W. H. Miller and B. M. D. D. Jansen op de Haar, *J. Chem. Phys.* **86**, 6213 (1987).
- [8] N. Rohringer, A. Gordon, and R. Santra, *Phys. Rev. A* **74**, 043420 (2006).
- [9] A. R. Edmonds, *Angular momentum in quantum mechanics* (Princeton University Press, 2016).
- [11] H.-J. Werner, P. J. Knowles, G. Knizia, F. R. Manby, M. Schütz, P. Celani, T. Korona, R. Lindh, A. Mitrushenkov, G. Rauhut, K. R. Shamasundar, T. B. Adler, R. D. Amos, A. Bernhardsson, A. Berning, D. L. Cooper, M. J. O. Deegan, A. J. Dobbyn, F. Eckert, E. Goll, C. H. I, A. Hesselmann, G. Hetzer, T. Hrenar, G. Jansen, C. Köppl, Y. Liu, A. W. Lloyd, R. A. Mata, A. J. May, S. J. McNicholas, W. Meyer, M. E. Mura, A. Nicklass, D. P. O’Neill, P. Palmieri, D. Peng, K. Pflüger, R. Pitzer, M. Reiher, T. Shiozaki, H. Stoll, A. J. Stone, R. Tarroni, T. Thorsteinsson, and M. Wang, “Molpro, version 2012.1, a package of ab initio programs.” .
- [12] H.-J. Werner, P. J. Knowles, G. Knizia, F. R. Manby, and M. Schtz, *Wiley Interdisciplinary Reviews: Computational Molecular Science* **2**, 242 (2012).
- [28] M. Shapiro and P. Brumer, *Rep. Prog. Phys.* **66**, 859

- (2003).
- [29] M. Shapiro and P. Brumer, *Quantum control of molecular processes* (John Wiley & Sons, 2012).
- [30] R. A. Kendall, T. H. Dunning Jr., and R. J. Harrison, *J. Chem. Phys.* **96**, 6796 (1992).
- [31] N. Douguet, A. N. Grum-Grzhimailo, E. V. Gryzlova, E. I. Staroselskaya, J. Venzke, and K. Bartschat, *Phys. Rev. A* **93**, 033402 (2016).
- [32] N. Douguet, A. N. Grum-Grzhimailo, and K. Bartschat, *Phys. Rev. A* **95**, 013407 (2017).
- [33] P. V. Demekhin, A. N. Artemyev, A. Kastner, and T. Baumert, arXiv:1807.01097 (2018).
- [34] D. Tannor and S. Rice, *J. Chem. Phys.* **83**, 5013 (1985).
- [35] D. J. Tannor, R. Kosloff, and S. A. Rice, *J. Chem. Phys.* **85**, 5805 (1986).

Supplemental material for Quantum control of photoelectron circular dichroism

R. Esteban Goetz,¹ Christiane P. Koch,² and Loren Greenman^{1,*}

¹*Department of Physics, Kansas State University,
116 Cardwell Hall, 1228 N. 17th St. Manhattan, KS 66506-2601*

²*Theoretische Physik, Universität Kassel, Heinrich-Plett-Str. 40, D-34132 Kassel, Germany*

(Dated: December 16, 2018)

For completeness, we provide here the details of the derivation of the orientation-averaged experimental observables, i.e., the anisotropy parameters and photoelectron circular dichroism (PECD), within the framework of second-order time-dependent perturbation approximation. Section I introduces the equations of motion for the electron dynamics and describes the perturbation treatment of the light-matter interaction. It also summarizes the operations needed to express the photoelectron momentum distribution in the laboratory frame of reference. Section II defines the orientation averaged laboratory-frame anisotropy parameters for the one-photon and two-photon ionization pathways and their interference. In Sec. III the symmetry properties of the different anisotropy parameters under polarization reversal are analyzed, and the PECD is defined accordingly. Section IV presents the optimization algorithm and cost functional.

Section V introduces the concept of “hemisphere-averaged PECD”, corresponding to a particular case of angle-integrated PECD, complementing the single- and two-photon PECD presented in Fig. 1(b) in the manuscript.

Section VI provides the time-frequency analysis (Wigner distribution function) of the fully-optimized pulse presented in the main text, allowing for disentangling the optimal multiple-two-photon ionization scheme from all possible two-photon pathways, further extending the analysis presented in the manuscript. The time-frequency analysis is accompanied by a more extended and detailed discussion of the three possible scenarios defined by the time-delay between the low and high frequency components of the fully optimized field presented in the manuscript.

Section VII complements Fig. 2 of the main text (with a final photoelectron energy of 6.5) by showing the corresponding results at a different photoelectron energy 10 eV, for which the largest PECD with bichromatic control is obtained. Section VII also discusses the role of the number of different two-photon ionization pathways probing different orbitals but interfering at a common photoelectron kinetic energy to maximize the PECD, and provides a study of the PECD as a function of the relative phase between the fundamental and second harmonic for a bichromatic $(\omega, 2\omega)$ pulse. Finally, sections VIII and IX contain the input file parameters for the electronic structure and scattering calculations, respectively.

I. PERTURBATION EXPANSION

A. Equations of motion

Equations (1) and (2) of the main text introduce the time-dependent many-electron Schrödinger equation and the expansion of the many-electron state $|\Psi^N(t)\rangle$ into the Hartree-Fock (HF) ground state and one-particle-one-hole excitations, $|\Phi_i^a\rangle$. The Slater determinant describing the HF ground-state is constructed from an anti-symmetric product of one-electron spin-orbitals φ_i ,

$$\Phi_0 = \mathcal{A} \prod_{i=1}^N \varphi_i(\mathbf{r}_i) \quad (1)$$

such that $\hat{\mathbf{H}}_0|\varphi_p\rangle = \epsilon_p|\varphi_p\rangle$ where ϵ_p are the orbital energies. Expanding the many-electron Hamiltonian into the basis of HF ground state and one-particle-one-hole excitations, defining

$$\begin{aligned} \epsilon_0 &= \langle \Phi_0 | \hat{\mathbf{H}}_0 | \Phi_0 \rangle, \\ \epsilon_i^a &= \langle \Phi_i^a | \hat{\mathbf{H}}_0 | \Phi_i^a \rangle \\ &= \epsilon_0 + \epsilon_a - \epsilon_i, \end{aligned} \quad (2)$$

and applying Brillouin’s theorem [1],

$$\langle \Phi_0 | \hat{\mathbf{H}}_1 | \Phi_i^a \rangle = 0, \quad (3)$$

we arrive at a set of coupled equations for the expansion coefficients,

$$\begin{aligned} \dot{\alpha}_0(t) &= i\mathcal{E}(t) \left[\langle \Phi_0 | \hat{\mathbf{r}} | \Phi_0 \rangle \alpha_0(t) \right. \\ &\quad \left. + \sum_{i,a} \langle \Phi_0 | \hat{\mathbf{r}} | \Phi_i^a \rangle e^{-i(\epsilon_i^a - \epsilon_0)t} \alpha_i^a(t) \right] \end{aligned} \quad (4a)$$

$$\begin{aligned} \dot{\alpha}_i^a(t) &= i\mathcal{E}(t) \left[\langle \Phi_i^a | \hat{\mathbf{r}} | \Phi_0 \rangle e^{-i(\epsilon_0 - \epsilon_i^a)t} \alpha_0(t) \right. \\ &\quad \left. + \sum_{j,b} \langle \Phi_i^a | \hat{\mathbf{r}} | \Phi_j^b \rangle e^{-i(\epsilon_j^b - \epsilon_i^a)t} \alpha_j^b(t) \right] \\ &\quad - i \sum_{j,b} \langle \Phi_i^a | \hat{\mathbf{H}}_1 | \Phi_j^b \rangle \alpha_j^b(t) e^{-(\epsilon_j^b - \epsilon_i^a)t}. \end{aligned} \quad (4b)$$

In particular, for $a = \mathbf{k}$, the coefficients $\alpha_i^{\mathbf{k}}(t)$ describe the transition amplitude from an initially occupied orbital i to a continuum state with energy $\epsilon_{\mathbf{k}} = |\mathbf{k}|^2/2$ in the direction $\mathbf{k}/|\mathbf{k}|$ with respect to the molecular frame of reference, \mathcal{R} . Similarly, $\alpha_i^{\mathbf{k}'}(t)$ describe this transition in the laboratory frame, \mathcal{R}' .

B. Orientation-averaged momentum distribution

The orientation-averaged momentum distribution of photoelectrons with energy ϵ_k emitted within a solid angle $d\Omega_{\mathbf{k}'}$ measured in the laboratory frame is given by Eq. (3) of the main text. In order to account for first- and second-order processes and their interference, we solve the equation of motion for the amplitudes $\alpha_i^{\mathbf{k}'}(t; \gamma_{\mathcal{R}})$ using second-order time-dependent perturbation theory which results in Eq. (4) of the main text. We limit the calculations to the single-channel approximation with i_0 labeling the HOMO orbital. The angle and energy resolved photoelectron distribution can then be written in terms of the contributions from one- and two-photon ionization processes and their interference,

$$\frac{d^2\sigma^{(\mu_0)}}{d\epsilon_k d\Omega_{\mathbf{k}'}} = \frac{d^2\sigma^{(\mu_0)1ph}}{d\epsilon_k d\Omega_{\mathbf{k}'}} + \frac{d^2\sigma^{(\mu_0)2ph}}{d\epsilon_k d\Omega_{\mathbf{k}'}} + \frac{d^2\sigma^{(\mu_0)int}}{d\epsilon_k d\Omega_{\mathbf{k}'}} \quad (5)$$

where $\mu_0 = (\pm 1, 0)$ defines the spherical unit vector components of the polarization direction \mathbf{e}'_{μ_0} in \mathcal{R}' . It has been introduced to distinguish the photoelectron distribution obtained with left ($\mu_0 = +1$) and right ($\mu_0 = -1$) circularly polarized light or with linear ($\mu_0 = 0$) polarization. The contribution from one-photon processes in Eq. (5) becomes

$$\begin{aligned} \frac{d^2\sigma^{(\mu_0)1ph}}{d\epsilon_k d\Omega_{\mathbf{k}'}} &= \int \alpha_{i_0}^{(1)\mathbf{k}'}(t; \gamma_{\mathcal{R}}) \alpha_{i_0}^{*(1)\mathbf{k}'}(t; \gamma_{\mathcal{R}}) d^3\gamma_{\mathcal{R}} \quad (6) \\ &= \sum_{L,M} \beta_{L,M}^{(\mu_0)1ph}(\epsilon_k) P_L^M(\cos\theta_{\mathbf{k}'}) e^{iM\phi_{\mathbf{k}'}} \end{aligned}$$

where in the second line we have invoked an expansion into associate Legendre polynomials, $P_L^M(\cdot)$. Similarly, contributions to the photoelectron momentum distribution originating from second-order order processes read

$$\begin{aligned} \frac{d^2\sigma^{(\mu_0)2ph}}{d\epsilon_k d\Omega_{\mathbf{k}'}} &= \int \alpha_{i_0}^{(2)\mathbf{k}'}(t; \gamma_{\mathcal{R}}) \alpha_{i_0}^{*(2)\mathbf{k}'}(t; \gamma_{\mathcal{R}}) d^3\gamma_{\mathcal{R}} \quad (7) \\ &= \sum_{L,M} \beta_{L,M}^{(\mu_0)2ph}(\epsilon_k) P_L^M(\cos\theta_{\mathbf{k}'}) e^{iM\phi_{\mathbf{k}'}} \end{aligned}$$

For the interference terms between one- and two-photon ionization pathways in Eq. (4) of the main text, we define

$$\beta_{L,M}^{(\mu_0)int} = \int \alpha_{i_0}^{(1)\mathbf{k}'}(\gamma_{\mathcal{R}}) \alpha_{i_0}^{*(2)\mathbf{k}'}(\gamma_{\mathcal{R}}) d^3\gamma_{\mathcal{R}} \quad (8)$$

Using Eq. (8), the contribution from the interfering pathways to the photoelectron spectrum reads

$$\begin{aligned} \frac{d^2\sigma^{(\mu_0)int}}{d\epsilon_k d\Omega_{\mathbf{k}'}} &= \int \left(\alpha_{i_0}^{(1)\mathbf{k}'}(t; \gamma_{\mathcal{R}}) \alpha_{i_0}^{*(2)\mathbf{k}'}(t; \gamma_{\mathcal{R}}) + c.c. \right) d^3\gamma_{\mathcal{R}} \\ &= \sum_{L,M} \left(\beta_{L,M}^{(\mu_0)int}(\epsilon_k) e^{iM\phi_{\mathbf{k}'}} + c.c. \right) P_L^M(\cos\theta_{\mathbf{k}'}) \end{aligned}$$

or, equivalently,

$$\begin{aligned} \frac{d^2\sigma^{(\mu_0)int}}{d\epsilon_k d\Omega_{\mathbf{k}'}} &= 2 \sum_{L,M} \left[\text{Re}[\beta_{L,M}^{(\mu_0)int}(\epsilon_k)] \cos(M\phi_{\mathbf{k}'}) \quad (9) \right. \\ &\quad \left. - \text{Im}[\beta_{L,M}^{(\mu_0)int}(\epsilon_k)] \sin(M\phi_{\mathbf{k}'}) \right] P_L^M(\cos\theta_{\mathbf{k}'}) \end{aligned}$$

where the possible values of L and M are determined by μ_0 as well as the symmetry properties after the orientation averaging. The portion of the photoelectron spectrum due to the interference term is sensitive to the relative phase between one- and two-photon processes. In particular, measurements on the (z', y') -plane ($\phi_{\mathbf{k}'} = \pi/2$) and (z', x') -plane ($\phi_{\mathbf{k}'} = 0$) may allow reconstruction of the phase.

C. First-order corrections

The first order correction of $\alpha_0(t)$ in Eq. (4a) reads

$$\begin{aligned} \alpha_0^{(1)}(t) &= i \langle \Phi_0 | \hat{\mathbf{r}} | \Phi_0 \rangle \int_{-\infty}^t \mathcal{E}(t') \alpha_0^{(0)}(t') dt' \quad (10) \\ &\quad + i \sum_{i,a} \langle \Phi_0 | \hat{\mathbf{r}} | \Phi_i^a \rangle \int_{-\infty}^t e^{-i(\epsilon_i^a - \epsilon_0)t'} \alpha_i^{a(0)}(t') \mathcal{E}(t') dt' \end{aligned}$$

where j in $\alpha_0^{(j)}(t)$ and $\alpha_i^{a(j)}(t)$ indicates the perturbation order. For convenience, both one-particle one-hole excitation to virtual bound and scattering states are contained in the index a in Eq. (10). Using the zeroth order approximations $\alpha_0^{(0)}(t) \approx 1$ and $\alpha_i^{a(0)}(t) \approx 0$, Eq. (10) becomes

$$\alpha_0^{(1)}(t) = i \langle \Phi_0 | \hat{\mathbf{r}} | \Phi_0 \rangle \int_{-\infty}^t \mathcal{E}(t') dt' \quad (11)$$

The first order correction for the one-particle one-hole excitations reads

$$\begin{aligned} \alpha_i^{a(1)}(t) &= i \langle \Phi_i^a | \hat{\mathbf{r}} | \Phi_0 \rangle \int_{-\infty}^t \alpha_0^{(0)}(t') e^{-i(\epsilon_0 - \epsilon_i^a)t'} \mathcal{E}(t') dt' \quad (12) \\ &\quad + i \sum_{j,b} \langle \Phi_i^a | \hat{\mathbf{r}} | \Phi_j^b \rangle \int_{-\infty}^t \alpha_j^{b(0)}(t') e^{-i(\epsilon_j^b - \epsilon_i^a)t'} \mathcal{E}(t') dt' \\ &\quad - i \sum_{j,b} \langle \Phi_i^a | \hat{\mathbf{H}}_1 | \Phi_j^b \rangle \int_{-\infty}^t e^{-i(\epsilon_j^b - \epsilon_i^a)t'} \alpha_j^{b(0)}(t') dt' \end{aligned}$$

Using again $\alpha_0^{(0)}(t) \approx 1$ and $\alpha_j^{a(0)}(t) \approx 0$, Eq. (12) reduces to

$$\alpha_i^{a(1)}(t) = i \langle \Phi_i^a | \hat{\mathbf{r}} | \Phi_0 \rangle \int_{-\infty}^t e^{-i(\epsilon_0 - \epsilon_i^a)t'} \mathcal{E}(t') dt' \quad (13)$$

where the two determinants differ only by one spin-orbital. Application of the Slater-Condon rules for one-electron operators \mathcal{O} [2],

$$\begin{aligned} \langle \Phi_0 | \hat{\mathcal{O}} | \Phi_0 \rangle &= \sum_i \langle \varphi_i | \hat{\mathcal{O}} | \varphi_i \rangle \\ \langle \Phi_0 | \hat{\mathcal{O}} | \Phi_i^a \rangle &= \langle \varphi_i | \hat{\mathcal{O}} | \varphi_a \rangle \end{aligned} \quad (14)$$

to Eq. (13) allows us to write the matrix elements in terms of the HF one-electron spin-orbitals,

$$\alpha_i^{a(1)}(t) = i \langle \varphi_a | \hat{\mathbf{r}} | \varphi_i \rangle \int_{-\infty}^t e^{-i(\epsilon_0 - \epsilon_i^a)t'} \mathcal{E}(t') dt' \quad (15)$$

with φ_s the s th occupied or unoccupied spin-orbital, cf. Eq. (1). In particular, the first-order correction for the quantity of interest, namely $\alpha_{i_0}^k(t)$, reads

$$\alpha_{i_0}^{k(1)}(t) = i \langle \Phi_{i_0}^k | \hat{\mathbf{r}} | \Phi_0 \rangle \int_{-\infty}^t e^{-i(\epsilon_0 - \epsilon_{i_0}^k)t'} \mathcal{E}(t') dt', \quad (16)$$

Assuming no relaxation of the contributing orbitals, the total wave function $\Phi_i^k(\mathbf{r}_N)$ can be defined, for any $i \in \text{occ}$, as an antisymmetrized product,

$$\Phi_i^k(\mathbf{r}_1, \dots, \mathbf{r}_N) = \mathcal{A}_N [\varphi_{\mathbf{k}}^-(\mathbf{r}_N); \Phi_i(\mathbf{r}_1, \dots, \mathbf{r}_{N-1})], \quad (17)$$

where $\varphi_{\mathbf{k}}^-(\mathbf{r}_N)$ is the scattering portion of the wave function and $\Phi_i(\mathbf{r}_1, \dots, \mathbf{r}_{N-1})$ the $N-1$ electron final state after ionization. We obtain $\varphi_{\mathbf{k}}^-(\mathbf{r})$ by solving the scattering problem

$$\left[-\frac{\nabla^2}{2} - \frac{1}{r} + \hat{\mathbf{V}} - \frac{k^2}{2} \right] \varphi_{\mathbf{k}}^-(\mathbf{r}) = 0, \quad (18)$$

with scattering boundary conditions [3, 4] for the outgoing wave $\varphi_{\mathbf{k}}^-(\mathbf{r})$ at large distances $\mathbf{r} \rightarrow \infty$, and where $\hat{\mathbf{V}}(\mathbf{r})$ describes the short-range part of the electron-ion interaction. Equation (18) including its matrix and tensor elements are computed using a locally modified version of the ePolyScat program package [5–7]. The orthogonality between the Hartree-Fock orbitals and scattering states obtained from the scattering calculations have been numerically verified within the tolerance range.

D. Second-order corrections

The second order correction of $\alpha_i^k(t)$ for $i \in \text{occ}$ is, according to Eq. (4b),

$$\begin{aligned} \alpha_i^{k(2)}(t) = & i \langle \Phi_{i_0}^k | \hat{\mathbf{r}} | \Phi_0 \rangle \int_{-\infty}^t e^{i(\epsilon_i^k - \epsilon_0)t'} \mathcal{E}(t') \alpha_0^{(1)}(t') dt' \quad (19) \\ & + i \sum_{j,b} \langle \Phi_{i_0}^k | \hat{\mathbf{r}} | \Phi_j^b \rangle \int_{-\infty}^t e^{i(\epsilon_i^k - \epsilon_j^b)t'} \mathcal{E}(t') \alpha_j^{b(1)}(t') dt' \\ & - i \sum_{j,b} \langle \Phi_{i_0}^k | \hat{\mathbf{H}}_1 | \Phi_j^b \rangle \int_{-\infty}^t e^{i(\epsilon_i^k - \epsilon_j^b)t'} \alpha_j^{b(1)}(t') dt'. \end{aligned}$$

The electron-correlation effects described by $\hat{\mathbf{H}}_1$ will be neglected. However, the exchange and Coulomb operator in $\hat{\mathbf{H}}_0$ ensure the excited electron to still experience a (chiral) Coulomb attraction to the residual cation [8]. To verify the chiral origin of PECD when $\hat{\mathbf{H}}_1$ is ignored, we have performed the same calculations using the achiral CH_4 and N_2 molecules, for which no PECD was observed (below machine precision).

Matrix elements are obtained using the rules for one-electron operators (14) together with

$$\begin{aligned} \langle \Phi_i^a | \hat{\mathbf{r}} | \Phi_j^b \rangle = & \delta_{a,b} (1 - \delta_{i,j}) \langle \varphi_a | \hat{\mathbf{r}} | \varphi_b \rangle \\ & + \delta_{i,j} (1 - \delta_{a,b}) \langle \varphi_j | \hat{\mathbf{r}} | \varphi_i \rangle \\ & + \delta_{i,j} \delta_{a,b} \sum_{r \in \{m_i^a\}} \langle \varphi_r | \hat{\mathbf{r}} | \varphi_r \rangle, \quad (20) \end{aligned}$$

with $\{m_i^a\} = \{1, \dots, i-1, a, i+1, \dots, N\}$. We restrict ourselves to the frozen-core approximation for the photoionization processes, allowing only the HOMO orbital, φ_{i_0} , to contribute to the photoionization via direct (first order) or two-photon (second order) ionization probing different unoccupied orbitals φ_a .

Inserting the first order corrections $\alpha_0^{(0)}(t)$ and $\alpha_i^{a(0)}(t)$ defined in Eqs. (11) and (13) into Eq. (19) gives

$$\begin{aligned} \alpha_{i_0}^{k(2)}(t) = & - \langle \Phi_{i_0}^k | \hat{\mathbf{r}} | \Phi_0 \rangle \langle \Phi_0 | \hat{\mathbf{r}} | \Phi_0 \rangle \quad (21) \\ & \times \int_{-\infty}^t e^{i(\epsilon_{i_0}^k - \epsilon_0)t'} \mathcal{E}(t') \int_{-\infty}^{t'} \mathcal{E}(t'') dt'' dt' \\ & - \sum_{\substack{b \notin \text{occ} \\ j \in \text{occ}}} \langle \Phi_{i_0}^k | \hat{\mathbf{r}} | \Phi_j^b \rangle \langle \varphi_b | \hat{\mathbf{r}} | \varphi_j \rangle \int_{-\infty}^t e^{i(\epsilon_{i_0}^k - \epsilon_j^b)t'} \mathcal{E}(t') \\ & \times \int_{-\infty}^{t'} e^{i(\epsilon_j^b - \epsilon_0)t''} \mathcal{E}(t'') dt'' dt'. \end{aligned}$$

E. Orientation-dependent momentum distribution

Two steps are still required to compute the laboratory frame quantities $\alpha_{i_0}^{k'(1)}(t; \gamma_{\mathcal{R}})$ and $\alpha_{i_0}^{k'(2)}(t; \gamma_{\mathcal{R}})$. First, if $\mathcal{E}(t) = \mathcal{E}_{\mu_0}(t)$ is known in \mathcal{R}' , the component $\mathcal{E}_{\mu_0}(t)$ must be projected into the molecular frame in order to evaluate all tensor elements. The orientation of \mathcal{R} with respect to \mathcal{R}' is defined by the Euler angles $\gamma_{\mathcal{R}} = (\alpha, \beta, \gamma)$. The second step involves rotation of the photoelectron direction of emission from \mathcal{R} to \mathcal{R}' , which is performed using the inverse of the transformation used in step 1.

In \mathcal{R}' , the electric field is decomposed into the spherical unit vectors ϵ'_{μ} , with $\mu = \pm 1, 0$,

$$\mathcal{E}(t) = \sum_{\mu} \mathcal{E}_{\mu} \epsilon'_{\mu} = \sum_{\mu} (-1)^{\mu} \mathcal{E}_{\mu} \hat{\epsilon}'_{-\mu},$$

such that $\mathcal{E}(t) \cdot \hat{\epsilon}'_{\mu_0} = \mathcal{E}_{\mu_0}(t)$. We recall that $\mu_0 = \pm 1, 0$ defines the left (+1), right (-1) or linear (0) polarization direction of the field. The spherical unit vector $\hat{\epsilon}'_{\mu_0}$ can be written in terms of its molecular-frame counterparts, ϵ_{μ} ,

$$\hat{\epsilon}'_{\mu_0} = \sum_{\mu=\pm 1, 0} \mathcal{D}_{\mu, \mu_0}^{(1)}(\gamma_{\mathcal{R}}) \epsilon_{\mu}, \quad (22)$$

where $\mathcal{D}_{\mu, \mu_0}^{(1)}(\gamma_{\mathcal{R}})$ are the components of the Wigner rotation matrix. Rotations between the two coordinate systems, \mathcal{R} and \mathcal{R}' , are performed following the convention for the Wigner rotation matrices of Ref. [9]. The tensor operator $\hat{\mathbf{r}}$ is also projected into the spherical unit vectors in \mathcal{R} ,

$$\hat{\mathbf{r}} = \sum_{\mu} (-1)^{\mu} \hat{\mathbf{r}}_{\mu} \epsilon_{-\mu},$$

such that $\hat{\mathbf{r}} \cdot \epsilon_{\mu_0} = \hat{\mathbf{r}}_{\mu_0}$. Finally, in the molecular frame, the dipole interaction reads

$$\mathcal{E}(t) \cdot \hat{\mathbf{r}} = \mathcal{E}_{\mu_0}(t) \sum_{\mu} \mathcal{D}_{\mu, \mu_0}^{(1)*}(\gamma_{\mathcal{R}}) \hat{\mathbf{r}}_{\mu}$$

with $\mu = \pm 1, 0$ and the matrix elements of the interaction become

$$\begin{aligned} \mathcal{E}_{\mu_0}(t) \langle \varphi_p | \epsilon_{\mu_0}^{\prime*} \cdot \hat{\mathbf{r}} | \varphi_q \rangle &= \mathcal{E}_{\mu_0}(t) \\ &\times \sum_{\mu} \mathcal{D}_{\mu, \mu_0}^{(1)*}(\gamma_{\mathcal{R}}) \langle \varphi_p | \hat{\mathbf{r}}_{\mu} | \varphi_q \rangle, \end{aligned} \quad (23)$$

where φ_p, φ_q symbolize two arbitrary spin-orbitals, and Eq. (23) is also valid for scattering states. Here, the $z' > 0$ axis is defined by the propagation direction of

the laser beam, normal to the (x', y') -plane (polarization plane for $\mu_0 = \pm 1$).

The second type of rotation involves projection of the direction of photoelectron emission from the molecular to the laboratory frame. In the molecular frame, the direction of photoelectron emission is obtained by expanding the scattering wave function into spherical harmonics,

$$\varphi_{\mathbf{k}}^-(\mathbf{r}) = \sum_{\ell, m} \varphi_{\bar{\mathbf{k}}, \ell, m}^-(\mathbf{r}) Y_m^{\ell}(\theta_{\mathbf{k}}, \phi_{\mathbf{k}}), \quad (24)$$

where $\theta_{\mathbf{k}}$ and $\phi_{\mathbf{k}}$ correspond to the polar and azimuthal angles in the molecular frame. To obtain the anisotropy parameters, evaluation of the product of two spherical harmonics, $Y_m^{\ell}(\theta_{\mathbf{k}}, \phi_{\mathbf{k}}) Y_{m'}^{\ell'}(\theta_{\mathbf{k}}, \phi_{\mathbf{k}})$, is required. This can be done using the well known expression [2]

$$Y_m^{\ell}(\theta_{\mathbf{k}}, \phi_{\mathbf{k}}) Y_{m'}^{\ell'}(\theta_{\mathbf{k}}, \phi_{\mathbf{k}}) = (-1)^m \sum_L \tilde{\gamma}_{\ell, \ell'}^L Y_{m-m'}^L(\theta_{\mathbf{k}}, \phi_{\mathbf{k}}) \begin{pmatrix} \ell & \ell' & L \\ 0 & 0 & 0 \end{pmatrix} \begin{pmatrix} \ell & \ell' & L \\ m & -m' & m' - m \end{pmatrix}. \quad (25)$$

where

$$\tilde{\gamma}(\ell, \ell', L) \equiv \sqrt{\frac{(2L+1)}{4\pi} (2\ell+1)(2\ell'+1)}.$$

The last step consists in writing the direction of photoelectron emission — determined by $Y_{m-m'}^L(\theta_{\mathbf{k}}, \phi_{\mathbf{k}})$ appearing in the rhs of Eq. (25) — with respect to the laboratory frame. This is achieved using the inverse of the transformation (22),

$$\begin{aligned} Y_{m-m'}^L(\theta_{\mathbf{k}}, \phi_{\mathbf{k}}) &= \mathcal{D}^{-1} Y_{m-m'}^L(\theta', \phi') = \sum_{M'} \mathcal{D}_{M, m-m'}^{(L)\dagger}(\gamma_{\mathcal{R}}) Y_M^L(\theta_{\mathbf{k}'}, \phi_{\mathbf{k}'}) \\ &= \sum_{M'} (-1)^{m-m'-M} \mathcal{D}_{m'-m, -M}^L(\gamma_{\mathcal{R}}) Y_M^L(\theta_{\mathbf{k}'}, \phi_{\mathbf{k}'}), \end{aligned} \quad (26)$$

which allows us to write Eq. (25) as a function of the polar and azimuthal angles $\theta_{\mathbf{k}'}$ and $\phi_{\mathbf{k}'}$ in the laboratory frame. The reason for rotating the product of two spherical harmonics instead of evaluating the product of two rotated harmonics is two-fold: first, it results in a more compact expression of the anisotropy parameters, by writing the final expression as a product of three in-

stead of four Wigner rotation matrices, and secondly, it allows for a more straightforward analysis of the properties of the Wigner $3j$ symbols appearing in the anisotropy parameters under polarization reversal which is of interest when evaluating the PECD.

Finally, applying Eq. (26) to the spherical harmonics in the rhs of Eq. (25) gives

$$Y_m^{\ell}(\theta_{\mathbf{k}}, \phi_{\mathbf{k}}) Y_{m'}^{\ell'}(\theta_{\mathbf{k}}, \phi_{\mathbf{k}}) = (-1)^{m'} \sum_{L, M} \tilde{\gamma}_{\ell, \ell'}^L \begin{pmatrix} \ell & \ell' & L \\ 0 & 0 & 0 \end{pmatrix} \begin{pmatrix} \ell & \ell' & L \\ m & -m' & m' - m \end{pmatrix} (-1)^{-M} \mathcal{D}_{m'-m, -M}^L(\gamma_{\mathcal{R}}) Y_M^L(\theta_{\mathbf{k}'}, \phi_{\mathbf{k}'})$$

or, equivalently,

$$Y_m^{\ell}(\theta_{\mathbf{k}}, \phi_{\mathbf{k}}) Y_{m'}^{\ell'}(\theta_{\mathbf{k}}, \phi_{\mathbf{k}}) = (-1)^{m'} \sum_{L, M} \zeta_{\ell, \ell'}^{L, M} \begin{pmatrix} \ell & \ell' & L \\ 0 & 0 & 0 \end{pmatrix} \begin{pmatrix} \ell & \ell' & L \\ m & -m' & m' - m \end{pmatrix} \mathcal{D}_{m'-m, -M}^L(\gamma_{\mathcal{R}}) P_L^M(\cos \theta_{\mathbf{k}'}) e^{iM\phi_{\mathbf{k}'}} , \quad (27)$$

where $P_L^M(\cdot)$ denotes the associate Legendre polynomials

and

$$\zeta_{\ell, \ell'}^{L, M} = \frac{(2L+1)}{4\pi} \sqrt{(2\ell+1)(2\ell'+1)} \frac{(L-M)!}{(L+M)!}. \quad (28)$$

The orientation-averaged laboratory-frame anisotropy parameters associated to the one- and two-photon ionization pathways and their interference defined in Sec. IB are evaluated in the following.

II. LABORATORY-FRAME ANISOTROPY PARAMETERS

A. Anisotropy parameters $\beta_{L,M}^{(\mu_0)1ph}$

Using Eq. (23), the molecular-frame Eq. (16) becomes

$$\alpha_{i_0}^{k(1)}(t; \gamma_{\mathcal{R}}) = i \sum_{\mu} \langle \Phi_{i_0}^k | \hat{\mathbf{r}}_{\mu} | \Phi_0 \rangle \mathcal{D}_{\mu, \mu_0}^{*(1)}(\gamma_{\mathcal{R}}) \times \int_{-\infty}^t e^{-i(\epsilon_{i_0}^k - \epsilon_0)t'} \mathcal{E}_{\mu_0}(t') dt' . \quad (29)$$

$$\begin{aligned} \alpha_{i_0}^{k'(1)}(\gamma_{\mathcal{R}}) \alpha_{i_0}^{*k'(1)}(\gamma_{\mathcal{R}}) &= (-1)^{-\mu_0} \sum_{\mu, \mu'} \sum_{\substack{\ell, m \\ \ell', m'}} \mathcal{M}_{k, \ell, m}^{\mu} \mathcal{M}_{k', \ell', m'}^{*\mu'} \int_{-\infty}^t e^{i(\epsilon_{i_0}^k - \epsilon_0)t'} \mathcal{E}_{\mu_0}(t') dt' \int_{-\infty}^t e^{-i(\epsilon_{i_0}^{k'} - \epsilon_0)t'} \mathcal{E}_{\mu_0}^*(t') dt' \\ &\times \sum_{L, M} \tilde{\gamma}_{\ell, \ell'}^{L, M} (-1)^{-m' + \mu} \begin{pmatrix} \ell & \ell' & L \\ 0 & 0 & 0 \end{pmatrix} \begin{pmatrix} \ell & \ell' & L \\ m & -m' & m' - m \end{pmatrix} P_L^M(\cos \theta_{\mathbf{k}'}) e^{iM\phi_{\mathbf{k}'}} \\ &\times \mathcal{D}_{-\mu, -\mu_0}^{(1)}(\gamma_{\mathcal{R}}) \mathcal{D}_{\mu', \mu_0}^{(1)}(\gamma_{\mathcal{R}}) \mathcal{D}_{m' - m, -M}^{(L)}(\gamma_{\mathcal{R}}) . \end{aligned} \quad (31)$$

We recall that $\mu_0 = \pm 1, 0$ defines the light polarization direction in the laboratory frame. Following Eq. (6), integrating Eq. (31) over the Euler angles leads to the contribution of the one-photon pathway to the momentum distribution. Integrating a product of three Wigner $3j$ -symbols over the Euler angles can be evaluated according to [9]

$$\begin{aligned} \int \mathcal{D}_{m_1, m'_1}^{(\ell_1)}(\gamma_{\mathcal{R}}) \mathcal{D}_{m_2, m'_2}^{(\ell_2)}(\gamma_{\mathcal{R}}) \mathcal{D}_{m_3, m'_3}^{(\ell_3)}(\gamma_{\mathcal{R}}) \frac{d^3 \gamma_{\mathcal{R}}}{8\pi^2} \\ = \begin{pmatrix} \ell_1 & \ell_2 & \ell_3 \\ m_1 & m_2 & m_3 \end{pmatrix} \begin{pmatrix} \ell_1 & \ell_2 & \ell_3 \\ m'_1 & m'_2 & m'_3 \end{pmatrix} . \end{aligned} \quad (32)$$

Inserting the partial wave expansion (24), we find

$$\begin{aligned} \alpha_{i_0}^{k(1)}(t; \gamma_{\mathcal{R}}) &= i \sum_{\mu} \sum_{\ell, m} \mathcal{M}_{k, \ell, m}^{(1)} \mathcal{D}_{\mu, \mu_0}^{*(1)}(\gamma_{\mathcal{R}}) \\ &\times Y_m^{\ell}(\theta_{\mathbf{k}}, \phi_{\mathbf{k}}) \int_{-\infty}^t e^{-i(\epsilon_{i_0}^k - \epsilon_0)t'} \mathcal{E}_{\mu_0}(t') dt' , \end{aligned} \quad (30)$$

where $\mathcal{M}_{k, \ell, m}^{\mu} \equiv \langle \Phi_{i_0}^{k, \ell, m} | \hat{\mathbf{r}}_{\mu} | \Phi_0 \rangle$ is the partial wave decomposition of the matrix elements in Eq. (29). Making use of Eq. (27) and evaluating $\alpha_{i_0}^k(t; \gamma_{\mathcal{R}}) \alpha_{i_0}^{*k}(t; \gamma_{\mathcal{R}})$ results in

Another useful property concerns the product of two Wigner rotation matrices given by [9]

$$\begin{aligned} \mathcal{D}_{m_1, m'_1}^{(\ell_1)}(\gamma_{\mathcal{R}}) \mathcal{D}_{m_2, m'_2}^{(\ell_2)}(\gamma_{\mathcal{R}}) &= \sum_{\ell} (2\ell + 1) \mathcal{D}_{-m_{12}, -m'_{12}}^{*(j)}(\gamma_{\mathcal{R}}) \\ &\times \begin{pmatrix} \ell_1 & \ell_2 & \ell \\ m_1 & m_2 & -m_{12} \end{pmatrix} \begin{pmatrix} \ell_1 & \ell_2 & \ell \\ m'_1 & m'_2 & -m'_{12} \end{pmatrix} , \end{aligned} \quad (33)$$

with $m_{12} = m_1 + m_2$ and $m'_{12} = m'_1 + m'_2$. Upon integration of Eq. (31) over the Euler angles using Eq. (32) and equating the result with Eq. (6), the contribution from the one-photon ionization pathway to the orientation-averaged anisotropy parameters is obtained,

$$\begin{aligned} \beta_{L, M}^{(\mu_0)1ph}(\epsilon_{\mathbf{k}}) &= 2\pi (2L + 1) \sqrt{(2\ell + 1)(2\ell' + 1)} (-1)^{-\mu_0} \\ &\times \sum_{\mu, \mu'} \sum_{\substack{\ell, m \\ \ell', m'}} \mathcal{M}_{k, \ell, m}^{\mu} \mathcal{M}_{k', \ell', m'}^{*\mu'} \int_{-\infty}^t e^{i(\epsilon_{i_0}^k - \epsilon_0)t'} \mathcal{E}_{\mu_0}(t') dt' \int_{-\infty}^t e^{-i(\epsilon_{i_0}^{k'} - \epsilon_0)t'} \mathcal{E}_{\mu_0}^*(t') dt' \\ &\times (-1)^{-m' + \mu} \begin{pmatrix} \ell & \ell' & L \\ 0 & 0 & 0 \end{pmatrix} \begin{pmatrix} \ell & \ell' & L \\ m & -m' & m' - m \end{pmatrix} \begin{pmatrix} 1 & 1 & L \\ -\mu & \mu' & m' - m \end{pmatrix} \begin{pmatrix} 1 & 1 & L \\ -\mu_0 & \mu_0 & 0 \end{pmatrix} \delta_{M, 0} . \end{aligned} \quad (34)$$

Next, we analyze the symmetry properties of $\beta_{\ell, m}^{(\mu_0)1ph}$

under polarization reversal, i.e., $\mu_0 \rightarrow -\mu_0$, which is of

interest in view of defining the PECD in Sec. III. We start by considering the fourth $3j$ Wigner symbol in Eq. (34), which is the only polarization dependent term in Eq. (34), and denote it by $\mathcal{S}_{1ph}(\mu_0)$. Under polarization reversal, $\mu_0 \rightarrow -\mu_0$, $\beta_{L,0}^{(\mu_0)1ph}$ transforms to $\beta_{L,0}^{(-\mu_0)1ph}$, and

$$\begin{aligned} \mathcal{S}_{1ph}(-\mu_0) &= \begin{pmatrix} 1 & 1 & L \\ \mu_0 & -\mu_0 & 0 \end{pmatrix} = (-1)^{2+L} \begin{pmatrix} 1 & 1 & L \\ -\mu_0 & \mu_0 & 0 \end{pmatrix} \\ &= (-1)^L \mathcal{S}(+\mu_0), \end{aligned} \quad (35)$$

due to the symmetry property for the Wigner $3j$ symbols,

$$\begin{pmatrix} j_1 & j_2 & j \\ m_1 & m_2 & m \end{pmatrix} = (-1)^{j_1+j_2+j} \begin{pmatrix} j_1 & j_2 & j \\ -m_1 & -m_2 & -m \end{pmatrix}. \quad (36)$$

Since no other term depends on μ_0 , Eq. (35) implies

$$\beta_{L,0}^{(+\mu_0)1ph} = (-1)^L \beta_{L,0}^{(-\mu_0)1ph}. \quad (37)$$

For $\mu_0 = 0$ (linear polarization), $\mathcal{S}(\mu_0 = 0)$ allows for only even numbers $1 + 1 + L$ to be non-zero. Therefore $\beta_{L=1,M=0}^{(0)1ph} = 0$. Furthermore, for $\mu_0 = \pm 1$, $L = 1$ is the only contributing term (up to second order), as it should be, since both the third and fourth Wigner $3j$ symbol in Eq. (34) are non-zero only for $0 \leq L \leq 2$. This implies $\beta_{3,0}^{(\mu_0)1ph} = 0$. Finally, using Eq. (37), Eq. (6) becomes, under the exchange $\mu_0 \rightarrow -\mu_0$,

$$\begin{aligned} \frac{d^2 \sigma^{(-\mu_0)1ph}}{d\epsilon_k d\Omega_{\mathbf{k}'}} &= \sum_{L=0}^2 \beta_{L,0}^{(-\mu_0)1ph} P_L^0(\cos \theta_{\mathbf{k}'}) \\ &= \sum_{L=0}^2 (-1)^L \beta_{L,0}^{(\mu_0)1ph} P_L^0(\cos \theta_{\mathbf{k}'}). \end{aligned} \quad (38)$$

B. Anisotropy parameters $\beta_{L,M}^{(\mu_0)2ph}$

Rotating all tensor elements of the dipole interaction in Eq. (21) into the molecular frame leads to

$$\begin{aligned} \alpha_{i_0}^{\mathbf{k}(2)}(t; \gamma_{\mathcal{R}}) &= - \sum_{\mu, \mu'} \mathcal{D}_{\mu, \mu_0}^{*(1)}(\gamma_{\mathcal{R}}) \mathcal{D}_{\mu', \mu_0}^{*(1)}(\gamma_{\mathcal{R}}) \left[\langle \Phi_{i_0}^{\mathbf{k}} | \hat{\mathbf{r}}_{\mu} | \Phi_0 \rangle \langle \Phi_0 | \hat{\mathbf{r}}_{\mu'} | \Phi_0 \rangle \int_{-\infty}^t e^{i(\epsilon_{i_0}^{\mathbf{k}} - \epsilon_0)t'} \mathcal{E}_{\mu_0}(t') \int_{-\infty}^{t'} \mathcal{E}_{\mu_0}(t'') dt'' dt' \right. \\ &\quad \left. + \sum_{\substack{b \notin \text{occ} \\ j \in \text{occ}}} \langle \Phi_{i_0}^{\mathbf{k}} | \hat{\mathbf{r}}_{\mu} | \Phi_j^b \rangle \langle \Phi_j^b | \hat{\mathbf{r}}_{\mu'} | \Phi_0 \rangle \int_{-\infty}^t e^{i(\epsilon_{i_0}^{\mathbf{k}} - \epsilon_{i_0}^b)t'} \mathcal{E}_{\mu_0}(t') \int_{-\infty}^{t'} e^{i(\epsilon_{i_0}^b - \epsilon_0)t''} \mathcal{E}_{\mu_0}(t'') dt'' dt' \right]. \end{aligned} \quad (39)$$

In order to write the final expression as a product of three Wigner rotation matrices — for easy integration over the Euler angles — it is convenient to apply Eq. (33) to the two Wigner rotation matrices in Eq. (39). Defining two-photon tensor matrix elements,

$$T_{\mu, \mu'}^{i_0, r}(k, l, m) = \begin{cases} \langle \varphi_{k, \ell, m}^- | \hat{\mathbf{r}}_{\mu} | \varphi_{i_0} \rangle \langle \Phi_0 | \hat{\mathbf{r}}_{\mu'} | \Phi_0 \rangle, & \text{if } r = i_0 \\ \langle \varphi_{k, \ell, m}^- | \hat{\mathbf{r}}_{\mu} | \varphi_r \rangle \langle \varphi_r | \hat{\mathbf{r}}_{\mu'} | \varphi_{i_0} \rangle, & \text{if } r > i_0, \end{cases}$$

together with the control-dependent quantity

$$\zeta_{\mu_0}^{i_0, r}(t; k) = \begin{cases} \int_{-\infty}^t e^{(\epsilon_{i_0}^{\mathbf{k}} - \epsilon_0)t'} \mathcal{E}_{\mu_0}(t') \int_{-\infty}^{t'} \mathcal{E}_{\mu_0}(t'') dt'' dt', & \text{if } r = i_0 \\ \int_{-\infty}^t e^{(\epsilon_{i_0}^{\mathbf{k}} - \epsilon_{i_0}^r)t'} \mathcal{E}_{\mu_0}(t') \int_{-\infty}^{t'} e^{i(\epsilon_{i_0}^r - \epsilon_0)t''} \mathcal{E}_{\mu_0}(t'') dt'' dt', & \text{if } r > i_0, \end{cases} \quad (40)$$

Eq. (39) becomes

$$\alpha_{i_0}^{\mathbf{k}(2)}(t; \gamma_{\mathcal{R}}) = - \sum_{\mu, \mu'} \sum_{\ell, m} \sum_{r \geq i_0} T_{\mu, \mu'}^{i_0, r}(k, \ell, m) \zeta_{\mu_0}^{i_0, r}(t; k) \sum_{Q_1=0}^2 g_{\mu, \mu'}^{(Q_1)}(\mu_0) \mathcal{D}_{-\mu-\mu', 0}^{(Q_1)}(\gamma_{\mathcal{R}}) Y_m^{\ell}(\Omega_{\mathbf{k}}) \quad (41)$$

where

$$g_{\mu, \mu'}^{(Q_1)}(\mu_0) \equiv (2Q_1 + 1) \begin{pmatrix} 1 & 1 & Q_1 \\ \mu & \mu' & -\mu' - \mu \end{pmatrix} \begin{pmatrix} 1 & 1 & Q_1 \\ \mu_0 & \mu_0 & -2\mu_0 \end{pmatrix}.$$

Analogously to the first-order correction, multiplication of Eq. (41) with its complex conjugate, followed by rewriting the product $Y_m^{\ell}(\Omega_{\mathbf{k}}) Y_{m'}^{\ell' *}(\Omega_{\mathbf{k}})$ using Eq. (27),

we find

$$\begin{aligned}
|\alpha_{i_0}^{\mathbf{k}'(2)}(t; \gamma\mathcal{R})|^2 &= \sum_{\mu, \mu'} \sum_{\ell, m} \sum_{r \geq i_0} T_{\mu, \mu'}^{i_0, r}(k, \ell, m) \zeta_{\mu_0}^{i_0, r}(t; k) \sum_{Q_1=0}^2 g_{\mu, \mu'}^{(Q_1)}(\mu_0) \\
&\times \sum_{\nu, \nu'} \sum_{\ell', m'} \sum_{r' \geq i_0} T_{\nu, \nu'}^{i_0, r'}(k, \ell', m') \zeta_{\mu_0}^{i_0, r'}(t; k) \sum_{Q_2=0}^2 g_{\nu, \nu'}^{(Q_2)}(\mu_0) \\
&\times (-1)^{-m' - \nu' - \nu} \sqrt{(2\ell + 1)(2\ell' + 1)} \sum_{L, M} \begin{pmatrix} \ell & \ell' & L \\ 0 & 0 & 0 \end{pmatrix} \begin{pmatrix} \ell & \ell' & L \\ m & -m' & m' - m \end{pmatrix} \frac{(2L + 1)}{4\pi} \sqrt{\frac{(L - M)!}{(L + M)!}} \\
&\times \mathcal{D}_{-\mu' - \mu, -2\mu_0}^{(Q_1)}(\gamma\mathcal{R}) \mathcal{D}_{\nu' + \nu, 2\mu_0}^{(Q_2)}(\gamma\mathcal{R}) \mathcal{D}_{m' - m; -M}^{(L)}(\gamma\mathcal{R}) P_L^M(\cos \theta_{\mathbf{k}'}) e^{iM\phi_{\mathbf{k}'}}. \tag{42}
\end{aligned}$$

Using Eq. (32), integration of Eq. (42) over the Euler angles gives the anisotropy parameters $\beta_{L, M}^{(\mu_0)2ph}$, associated with the two-photon ionization process,

$$\begin{aligned}
\beta_{L, M}^{(\mu_0)2ph}(\epsilon_k) &= (2\pi)(2L + 1) \sum_{\mu, \mu'} \sum_{\ell, m} \sum_{r \geq i_0} T_{\mu, \mu'}^{i_0, r}(k, \ell, m) \zeta_{\mu_0}^{i_0, r}(t; k) \sum_{Q_1=0}^2 g_{\mu, \mu'}^{(Q_1)}(\mu_0) \\
&\times \sum_{\nu, \nu'} \sum_{\ell', m'} \sum_{r' \geq i_0} T_{\nu, \nu'}^{*i_0, r'}(k, \ell', m') \zeta_{\mu_0}^{*i_0, r'}(t; k) \sum_{Q_2=0}^2 g_{\nu, \nu'}^{(Q_2)}(\mu_0) \\
&\times (-1)^{-m' - \nu' - \nu} \sqrt{(2\ell + 1)(2\ell' + 1)} \\
&\times \begin{pmatrix} \ell & \ell' & L \\ 0 & 0 & 0 \end{pmatrix} \begin{pmatrix} \ell & \ell' & L \\ m & -m' & m' - m \end{pmatrix} \begin{pmatrix} Q_1 & Q_2 & L \\ -\mu' - \mu & \nu' + \nu & m' - m \end{pmatrix} \begin{pmatrix} Q_1 & Q_2 & L \\ -2\mu_0 & 2\mu_0 & -M \end{pmatrix} \delta_{M, 0} \tag{43}
\end{aligned}$$

with $\mu_0 = \pm 1, 0$. Since the last Wigner $3j$ symbol in Eq. (43) is non-zero only if $-2\mu_0 + 2\mu_0 - M = 0$, non-vanishing Legendre coefficients are possible only for $M = 0$. This translates into a symmetry of the photoelectron probability distribution around the z' axis.

We now evaluate the behavior of $\beta_{L, 0}^{(\mu_0)2ph}$ under helicity exchange $\mu_0 \rightarrow -\mu_0$. To this end, we define the fourth Wigner $3j$ symbol in Eq. (43) by $\mathcal{S}_{2ph}(\mu_0)$. Under helicity reversal, it transforms according to

$$\begin{aligned}
\mathcal{S}_{2ph}(-\mu_0) &= \begin{pmatrix} Q_1 & Q_2 & L \\ +2\mu_0 & -2\mu_0 & 0 \end{pmatrix} \\
&= (-1)^{Q_1 + Q_2 + L} \begin{pmatrix} Q_1 & Q_2 & L \\ -2\mu_0 & +2\mu_0 & 0 \end{pmatrix} \\
&= (-1)^{Q_1 + Q_2 + L} \mathcal{S}_{2ph}(+\mu_0). \tag{44}
\end{aligned}$$

Additional μ_0 -dependent quantities in Eq. (43) are $g_{\mu, \mu'}^{(Q_1)}(\mu_0)$ and $g_{\nu, \nu'}^{(Q_2)}(\mu_0)$, both transforming according to

$$\begin{aligned}
g_{\mu, \mu'}^{(Q_1)}(-\mu_0) &= (-1)^{Q_1} g_{\mu, \mu'}^{(Q_1)}(\mu_0) \\
g_{\nu, \nu'}^{(Q_2)}(-\mu_0) &= (-1)^{Q_2} g_{\nu, \nu'}^{(Q_2)}(\mu_0). \tag{45}
\end{aligned}$$

We thus find

$$\begin{aligned}
\mathcal{S}_{2ph}(-\mu_0) g_{\mu, \mu'}^{(Q_1)}(-\mu_0) g_{\nu, \nu'}^{(Q_2)}(-\mu_0) &= \\
(-1)^L \mathcal{S}_{2ph}(+\mu_0) \times g_{\mu, \mu'}^{(Q_1)}(+\mu_0) \times g_{\nu, \nu'}^{(Q_2)}(+\mu_0), &
\end{aligned}$$

which implies

$$\beta_{L, M}^{(-\mu_0)2ph}(\epsilon_k) = (-1)^L \beta_{L, M}^{(+\mu_0)2ph}(\epsilon_k). \tag{46}$$

Analogously to $\beta_{L, 0}^{(\mu_0)1ph}$ and as expected, $\beta_{L, 0}^{(\mu_0)2ph}$ also changes sign only for odd L and remains unchanged for even L when $\mu_0 \rightarrow -\mu_0$. However, in contrast to $\beta_{L, 0}^{(\mu_0)1ph}$, for which the only odd contributing order was found to be $L = 1$, both $L = 1$ and $L = 3$ are allowed for $\beta_{L, M}^{(\mu_0)2ph}$. In fact, since $|Q_1 - Q_2| \leq L \leq Q_1 + Q_2$, cf. the fourth Wigner $3j$ symbol in Eq. (43), and because $0 \leq Q_1 \leq 2$ and $0 \leq Q_2 \leq 2$, the possible values for L are $0 \leq L \leq 4$. Finally, under polarization reversal, Eq. (7) becomes

$$\begin{aligned}
\frac{d^2 \sigma^{(-\mu_0)2ph}}{d\epsilon_k d\Omega_{\mathbf{k}'}} &= \sum_{L=0}^4 \beta_{L, 0}^{(-\mu_0)2ph}(\epsilon_k) P_L^0(\cos \theta_{\mathbf{k}'}) \\
&= \sum_{L=0}^4 (-1)^L \beta_{L, 0}^{(+\mu_0)2ph}(\epsilon_k) P_L^0(\cos \theta_{\mathbf{k}'}) . \tag{47}
\end{aligned}$$

C. Anisotropy parameters $\beta_{L,M}^{(\mu_0)int}$

Using Eq. (30) and Eq. (41) for the first and second order corrections, respectively, we obtain, after rotation

$$\begin{aligned}
\alpha_{i_0}^{k'(1)}(t; \gamma_{\mathcal{R}}) \alpha_{i_0}^{*k'(2)}(t; \gamma_{\mathcal{R}}) &= -\frac{i}{4\pi} (-1)^{-\mu_0} \sum_{\mu} \sum_{\ell, m} \mathcal{M}_{k, \ell, m}^{\mu} \int_{-\infty}^t e^{-i(\epsilon_{i_0}^k - \epsilon_0)} \mathcal{E}_{\mu_0}(t') dt' \\
&\times \sum_{\nu, \nu'} \sum_{\ell', m'} \sum_{r \geq i_0} \sum_{Q=0}^2 T_{\nu, \nu'}^{*i_0, r}(k, \ell', m') \zeta_{\mu_0}^{*i_0, r}(t; k) g_{\nu, \nu'}^{(Q)}(\mu_0) \\
&\times (-1)^{-m' + \mu - \nu' - \nu} \sum_{L=|\ell - \ell'|}^{\ell + \ell'} (2L + 1) \sqrt{(2\ell + 1)(2\ell' + 1)} \begin{pmatrix} \ell & \ell' & L \\ 0 & 0 & 0 \end{pmatrix} \begin{pmatrix} \ell & \ell' & L \\ m & -m' & m' - m \end{pmatrix} \\
&\times \sum_{M=-L}^L \sqrt{\frac{(L - M)!}{(L + M)!}} \left[\mathcal{D}_{-\mu, -\mu_0}^{(1)}(\gamma_{\mathcal{R}}) \mathcal{D}_{\nu' + \nu, 2\mu_0}^{(Q)}(\gamma_{\mathcal{R}}) \mathcal{D}_{m' - m, -M}^{(L)}(\gamma_{\mathcal{R}}) \right] \times P_L^M(\cos \theta_{\mathbf{k}'}) e^{iM\phi_{\mathbf{k}'}}.
\end{aligned} \tag{48}$$

Integrating Eq. (48) over the Euler angles gives the (complex) anisotropy parameters associated with the interference term, as defined in Eq. (8). Orientation averaging determines the possible values of M in Eq. (9). In fact, using the equality

$$\begin{aligned}
&\int \mathcal{D}_{-\mu, -\mu_0}^{(1)}(\gamma_{\mathcal{R}}) \mathcal{D}_{\nu' + \nu, 2\mu_0}^{(Q)}(\gamma_{\mathcal{R}}) \mathcal{D}_{m' - m, -M}^{(L)}(\gamma_{\mathcal{R}}) d^3\gamma_{\mathcal{R}} \\
&= 8\pi^2 \begin{pmatrix} 1 & Q & L \\ -\mu & \nu' + \nu & m' - m \end{pmatrix} \begin{pmatrix} 1 & Q & L \\ -\mu_0 & 2\mu_0 & -M \end{pmatrix},
\end{aligned} \tag{49}$$

it is apparent that the second Wigner $3j$ symbol in Eq. (49) is non-zero only if $-\mu_0 + 2\mu_0 - M = 0$. Consequently,

$$\begin{pmatrix} 1 & Q & L \\ -\mu_0 & 2\mu_0 & -M \end{pmatrix} = \begin{pmatrix} 1 & Q & L \\ -\mu_0 & 2\mu_0 & -\mu_0 \end{pmatrix} \delta_{-M, -\mu_0} \tag{50}$$

i.e., $M = \mu_0$. Therefore, Eq. (7) is reduced to

$$\frac{d^2\sigma^{(\mu_0)int}}{d\epsilon_k d\Omega_{\mathbf{k}'}} = \sum_{L=0}^3 \left[\beta_{L, \mu_0}^{(\mu_0)int}(\epsilon_k) e^{i\mu_0\phi_{\mathbf{k}'}} + \beta_{L, \mu_0}^{*(\mu_0)int}(\epsilon_k) e^{-i\mu_0\phi_{\mathbf{k}'}} \right] P_L^{\mu_0}(\cos \theta_{\mathbf{k}'}), \tag{51}$$

From Eq. (51), it is apparent that for $\mu_0 = \pm 1$, the portion of the momentum distribution due to the interference between one-photon and two-photon ionization pathways breaks the azimuthal symmetry of photoelectron emission around the light propagation direction z' . This is in contrast to the contributions from $\beta_{L,0}^{(\mu_0)1ph}$ and $\beta_{L,0}^{(\mu_0)2ph}$ which we found to be symmetric around z' . The anisotropy parameter due to interference is obtained upon the integration of Eq. (48) over the Euler angles using Eq. (49) and reads

$$\begin{aligned}
\beta_{L, \mu_0}^{(\mu_0)int}(\epsilon_k) &= -2i\pi (2L + 1) \sum_{\mu} \sum_{\ell, m} \mathcal{M}_{k, \ell, m}^{\mu} \int_{-\infty}^t e^{-i(\epsilon_{i_0}^k - \epsilon_0)} \mathcal{E}_{\mu_0}(t') dt' \times \sum_{\nu, \nu'} \sum_{\ell', m'} \sum_{r \geq i_0} \sum_{Q=0}^2 T_{\nu, \nu'}^{*i_0, r}(k, \ell', m') \zeta_{\mu_0}^{*i_0, r}(t; k) \\
&\times (-1)^{-m' + \mu - \nu' - \nu} \sqrt{(2\ell + 1)(2\ell' + 1)} \begin{pmatrix} \ell & \ell' & L \\ 0 & 0 & 0 \end{pmatrix} \begin{pmatrix} \ell & \ell' & L \\ m & -m' & m' - m \end{pmatrix} \begin{pmatrix} 1 & Q & L \\ -\mu & \nu' + \nu & m' - m \end{pmatrix} \\
&\times (-1)^{-\mu_0} g_{\nu, \nu'}^{(Q)}(\mu_0) \begin{pmatrix} 1 & Q & L \\ -\mu_0 & 2\mu_0 & -\mu_0 \end{pmatrix} \sqrt{\frac{(L - \mu_0)!}{(L + \mu_0)!}}
\end{aligned} \tag{52}$$

Since $Q = 0, 1, 2$, it is apparent from the fourth Wigner $3j$ symbol in Eq. (52) that $L = 4$ cannot contribute. Fur-

thermore, if $\mu_0 = \pm 1$, it also the $L = 0$ term vanishes, and the allowed values are $L = 1, 2, 3$ for circularly polarized light, which explains the upper limit in the summation over Q in Eq. (51).

The symmetry properties of $\beta_{L,M}^{(\mu_0)int}$ under polarization reversal are analyzed using the same technique as for the one-photon and two-photon terms. It is worth pointing out, however, that evaluation of symmetry properties of Eq. (51) under polarization reversal also requires evaluation of the angular functions under $\mu_0 \rightarrow -\mu_0$ if $\mu_0 = \pm 1$. As previously discussed, the term $g_{\nu,\nu'}^{(Q)}(\mu_0)$ in the rhs of Eq. (52) transforms according to

$$g_{\nu,\nu'}^{(Q)}(-\mu_0) = (-1)^Q g_{\nu,\nu'}^{(Q)}(+\mu_0). \quad (53a)$$

Analogously, the fourth Wigner $3j$ symbol in Eq. (52), denoted by $\mathcal{S}_{int}(\mu_0)$, changes, under $\mu_0 \rightarrow -\mu_0$, as

$$\begin{aligned} \mathcal{S}_{int}(-\mu_0) &\equiv \begin{pmatrix} 1 & Q & L \\ +\mu_0 & -2\mu_0 & +\mu_0 \end{pmatrix} \\ &= (-1)^{1+Q+L} \begin{pmatrix} 1 & Q & L \\ +\mu_0 & -2\mu_0 & +\mu_0 \end{pmatrix} \\ &= (-1)^{1+Q+L} \mathcal{S}(-\mu_0). \end{aligned} \quad (53b)$$

Finally, defining

$$\mathcal{B}(\mu_0) \equiv \sqrt{\frac{(L - \mu_0)!}{(L + \mu_0)!}},$$

it is straightforward to show that

$$\mathcal{B}(-\mu_0) = \mathcal{B}(\mu_0) \times \frac{(L + \mu_0)!}{(L - \mu_0)!}. \quad (53c)$$

Using Eqs. (53)(a)-(c), the anisotropy parameter $\beta_{L,-\mu_0}^{(-\mu_0)int}(\epsilon)$ behaves as

$$\beta_{L,-\mu_0}^{(-\mu_0)int} = (-1)^{1+L} \frac{(L - \mu_0)!}{(L + \mu_0)!} \times \beta_{L,+\mu_0}^{(+\mu_0)int} \quad (54)$$

For the azimuthal dependency of Eq. (51), the transformation under helicity exchange is trivial. As for the associated Legendre polynomials $P_L^{\mu_0}(\cdot)$, we use the well-known property

$$P_L^{-M}(X) = (-1)^{-M} \frac{(L - M)!}{(L + M)!} \times P_L^M(X), \quad (55)$$

which, together with Eq. (54), allows us to write the transformed Eq. (51), for $\mu_0 = \pm 1$,

$$\begin{aligned} \frac{d^2\sigma^{(-\mu_0)int}}{d\epsilon_k d\Omega_{\mathbf{k}'}} &= 2 \sum_{L=0}^3 (-1)^L \left[\cos(\mu_0 \phi_{\mathbf{k}'}) \text{Re}[\beta_{L,+\mu_0}^{(+\mu_0)int}] \right. \\ &\quad \left. + \sin(\mu_0 \phi_{\mathbf{k}'}) \text{Im}[\beta_{L,+\mu_0}^{(+\mu_0)int}] \right] P_L^{+\mu_0}(\cos \theta_{\mathbf{k}'}). \end{aligned} \quad (56)$$

III. PHOTOELECTRON CIRCULAR DICHROISM

The PECD is defined as the non-vanishing component of the differential photoelectron signal obtained with left and right circularly polarized light,

$$\text{PECD}(\epsilon_k, \theta_{\mathbf{k}'}, \phi_{\mathbf{k}'}) = \frac{d^2\sigma^{(\mu_0)}}{d\epsilon_k d\Omega_{\mathbf{k}'}} - \frac{d^2\sigma^{(-\mu_0)}}{d\epsilon_k d\Omega_{\mathbf{k}'}}. \quad (57)$$

Both terms on the rhs of Eq. (57) contain the contributions defined in Eq. (5), i.e. contributions from the one-photon and two-photon ionization pathways and their interference. Therefore, we can analyze the PECD associated with each of these pathways. In particular,

$$\begin{aligned} \frac{d^2\sigma^{(+\mu_0)1ph}}{d\epsilon_k d\Omega_{\mathbf{k}'}} - \frac{d^2\sigma^{(-\mu_0)1ph}}{d\epsilon_k d\Omega_{\mathbf{k}'}} &= \sum_j 2\beta_{2j+1,0}^{(\mu_0)1ph} P_{2j+1}^0(\cos \theta_{\mathbf{k}'}) \\ &= 2\beta_{1,0}^{(+\mu_0)1ph} P_1^0 \cos(\theta_{\mathbf{k}'}), \end{aligned} \quad (58a)$$

gives the contribution of the one-photon ionization pathways to the PECD. The contribution from the two-photon ionization pathways is obtained as

$$\begin{aligned} \frac{d^2\sigma^{(+\mu_0)2ph}}{d\epsilon_k d\Omega_{\mathbf{k}'}} - \frac{d^2\sigma^{(-\mu_0)2ph}}{d\epsilon_k d\Omega_{\mathbf{k}'}} &= 2\beta_{1,0}^{(+\mu_0)2ph} P_1^0 \cos(\theta_{\mathbf{k}'}) \\ &\quad + 2\beta_{3,0}^{(+\mu_0)2ph} P_3^0 \cos(\theta_{\mathbf{k}'}). \end{aligned} \quad (58b)$$

Finally, the contribution of the interference between one-photon and two-photon ionization pathways reads

$$\begin{aligned} \frac{d^2\sigma^{(+\mu_0)int}}{d\epsilon_k d\Omega_{\mathbf{k}'}} - \frac{d^2\sigma^{(-\mu_0)int}}{d\epsilon_k d\Omega_{\mathbf{k}'}} &= 4 \cos(\mu_0 \phi_{\mathbf{k}'}) \sum_j \text{Re}[\beta_{2j+1,+\mu_0}^{(+\mu_0)int}] P_{2j+1}^{+\mu_0}(\cos \theta_{\mathbf{k}'}) \\ &\quad - 4 \sin(\mu_0 \phi_{\mathbf{k}'}) \sum_j \text{Im}[\beta_{2j,+\mu_0}^{(+\mu_0)int}] P_{2j}^{+\mu_0}(\cos \theta_{\mathbf{k}'}). \end{aligned} \quad (58c)$$

Equation (58c) implies that, in the (z', y') -plane, i.e., for $\phi_{\mathbf{k}'} = \pi/2$, PECD due to the interference term depends on the associate Legendre polynomials of even order. PECD thus changes sign in the forward and backward direction defined by the intervals $\theta_{\mathbf{k}} \in [0, \pi/2]$ and $\theta_{\mathbf{k}} \in [\pi/2, \pi]$, respectively. Conversely, projection of Eq. (58c) into the (z', x') -plane leads to an odd-order dependency, which does not change sign between forward and backward directions. In fact, the associate Legendre polynomials are either even or odd according to

$$P_L^M(-X) = (-1)^{L+M} P_L^M(X) \quad (58d)$$

with $M \equiv \mu_0$ and where $X \equiv \cos(\theta_{\mathbf{k}'})$ changes sign in the forward and backward directions. Choosing $\phi_{\mathbf{k}'} = \pi/2$ and accounting for the fact that $L = 2$ is the possible even order for non-vanishing $\beta_{L,+\mu_0}^{(+\mu_0),int}$ for $\mu_0 = \pm 1$ as

discussed in Section II C, Eq. (58c) becomes

$$\begin{aligned} \left. \frac{d^2 \sigma^{(+1)int}}{d\epsilon_k d\Omega_{\mathbf{k}'}} - \frac{d^2 \sigma^{(-1)int}}{d\epsilon_k d\Omega_{\mathbf{k}'}} \right|_{\phi_{\mathbf{k}'} = \pi/2} & \quad (58e) \\ & = 6 \operatorname{Im}[\beta_{2,+1}^{(+1)int}] \sin(2\theta_{\mathbf{k}'}), \end{aligned}$$

where we have used $P_2^1(\cos \theta) = -3 \cos(\theta) \sin(\theta)$ together with the trigonometric identity $\sin(2\theta) = 2 \cos(\theta) \sin(\theta)$.

Finally, accounting for the contributions from one-photon and two-photon ionization pathways and their interference, given by Eqs. (58a), (58b) and (58e), Eq. (57) becomes

$$\begin{aligned} \text{PECD}(\epsilon_k, \theta_{\mathbf{k}'}, \phi_{\mathbf{k}'} = \pi/2) & = 2 [\beta_{1,0}^{(+1)1ph}(\epsilon_k) + \beta_{1,0}^{(+1)2ph}(\epsilon_k)] P_1^0(\cos \theta_{\mathbf{k}'}) \\ & + 2\beta_{1,0}^{(+1)2ph}(\epsilon_k) P_3^0(\cos \theta_{\mathbf{k}'}) + 6 \operatorname{Im}[\beta_{2,+1}^{(+1)int}(\epsilon_k)] \sin(2\theta_{\mathbf{k}'}). \end{aligned} \quad (59)$$

IV. CONTROL OF PECD

A. Optimization algorithm

In the following, we summarize the optimization algorithm.

- (a) In a first step, the driving control field, $\epsilon(t)$ is parametrized following Eq. (9) in the main text, imposing restrictions on the frequency components, amplitudes, etc. following the guidelines in Ref. [10].
- (b) The anisotropy parameters $\beta_{L,M}^{(+1)1ph}(\epsilon_k)$, $\beta_{L,M}^{(+1)2ph}(\epsilon_k)$, and $\beta_{L,M}^{(+1)int}(\epsilon_k)$ in Eq. (59) are obtained using Eq. (34), Eq. (43) and Eq. (52), respectively. The time-integration appearing in the anisotropy parameters is evaluated using the parametrized time-dependent control field defined in step (a).
- (c) The total photoelectron momentum distribution is then evaluated using Eq. (5). The individual terms are defined in Eqs. (6), (7) and (9). The maximum value of Eq. (5), \mathcal{N} , is used to normalize Eq. (59) if its value exceeds a given threshold, otherwise we set $\text{PECD} = 0$.

Note that, since the PECD is normalized with respect to the peak intensity of the photoelectron momentum distribution, also all the anisotropy parameters appearing in Eqs. (6), (7) and (9) must be evaluated according to the equations stated in step (b).

B. Control objective

If the final photoelectron energy ϵ_k^* is specified but the direction $\theta_{\mathbf{k}'}$ is not (for more flexibility), the control objective takes the form

$$\Gamma[\epsilon] = \max_{\theta_{\mathbf{k}'}} \left| \mathcal{N}^{-1} \text{PECD}(\epsilon_k = \epsilon_k^*, \theta_{\mathbf{k}'}, \phi_{\mathbf{k}'} = \pi/2) \right|, \quad (60)$$

where both PECD and \mathcal{N} depend on the control field $\epsilon(t)$.

Conversely, if the peak position in energy is not specified, the control objective reads

$$\Gamma'[\epsilon] = \max_{\epsilon_k, \theta_{\mathbf{k}'}} \left| \mathcal{N}^{-1} \text{PECD}(\epsilon_k, \theta_{\mathbf{k}'}, \phi_{\mathbf{k}'} = \pi/2) \right|, \quad (61)$$

which gives more flexibility than one would obtain by integrating over ϵ_k since the anisotropy parameters (that depends on ϵ_k) are in this case not forced to have large magnitude at all ϵ_k (only “the” maximum at a particular ϵ_k^* is of interest).

The functional is evaluated iteratively and the pulse parameters (required to evaluate the time-integrals in the anisotropy parameters) are iteratively updated using the adaptation of the Brent’s principal axis method to a sequential scheme detailed in Ref. [10].

V. SINGLE- AND TWO PHOTON ANGLE-INTEGRATED PECD

In Fig. 1(b) in the manuscript, we have reported the maximum the single- and two-photon PECD over all angles $\theta_{\mathbf{k}}$ as a function of the photoelectron energy, which correspond to the expression defined in Eq. (60), and where ϵ_k^* refers to the photoelectron energy defining the horizontal axis.

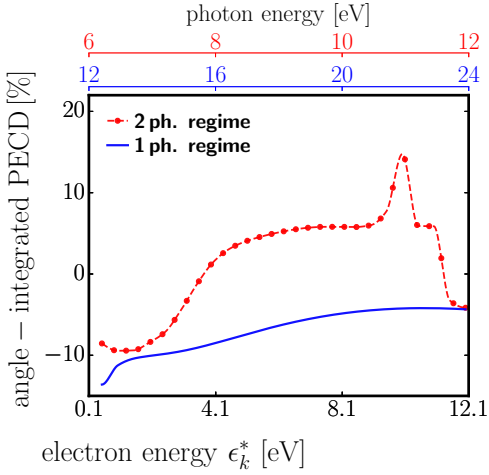


FIG. 4. Angle-averaged PECD obtained by integrating the PECD distribution in the forward hemisphere, defined by the light propagation direction along the z axis, cf. Fig. 1(a) in the manuscript.

As a complementary support, we provide here the “hemisphere-averaged” PECD, which corresponds to an angle-integrated (over the forward hemisphere) version of the PECD presented Fig. 1(b) in the manuscript. The forward (backward) “hemisphere-averaged” PECD is obtained by integrating the PECD distribution over the forward (backward) hemisphere. In the interest of consistency with Fig. 1(a) in the manuscript and Eq. (59)¹ in the supplemental material, the azimuthal direction of photoelectron emission defined by $\phi_{\mathbf{k}'}$, is kept fixed at $\phi_{\mathbf{k}'} = \pi/2$. In particular, the forward “hemisphere-averaged” PECD, $\rho_f(\epsilon_k)$, is evaluated by integrating the PECD distribution defined in Eq. (57), using the expression in Eq. (59), namely

$$\rho_f(\epsilon_k) = \int_0^{\pi/2} \text{PECD}(\epsilon_k, \theta_{\mathbf{k}'}, \phi_{\mathbf{k}'} = \pi/2) \sin \theta_{\mathbf{k}'} d\theta_{\mathbf{k}'}. \quad (62)$$

Conversely, the backward “hemisphere averaged” counterpart, $\rho_b(\epsilon_k)$, is obtained upon integrating the PECD distribution in the interval $\theta_{\mathbf{k}'} \in [\pi/2, \pi]$, with the property $\rho_b(\epsilon_k) = -\rho_f(\epsilon_k)$.

Figure 4 depicts the averaged PECD integrated over the forward hemisphere. For the sake of consistency with all PECD-related quantities presented in the manuscript, the forward “hemisphere-averaged” PECD shown in Fig. 4, is expressed in percentage of the peak photoelectron intensity.

VI. DISENTANGLING THE OPTIMAL TWO-PHOTON PATHWAY INTERFERENCE SCHEME FROM ALL POSSIBLE CONTRIBUTING TWO-PHOTON PATHWAYS

Analyzing the spectrum in Fig. 3(b) in the manuscript, we have identified all possible two-photon pathways leading to the same final photoelectron kinetic energy of 6.5 eV. The fully-optimized spectrum was found to contain specific frequencies components, ω_1 , ω_2 and ω_3 , which correspond, within a given width, to the transition energies ω_{0j} , for $j = 1, \dots, 4$, between the HOMO and LUMO + $j - 1$ orbitals. The field spectrum in Fig. 3(b) in the manuscript is characterized by a low (ω_1) and high (ω_2, ω_3) frequency components. Depending on the relative delay between these low and high frequency components –which may be viewed as a pump-probe scheme– three different scenarios may be considered. The goal here is to unravel which of these scenarios corresponds to the optimal scheme leading to a PECD of 68%.

The first scenario, \mathcal{S}_1 , consists in populating the LUMO orbital upon absorption of a photon with energy ω_{10} , which is available within the spectral width of the low frequency component ω_1 . This step can be followed by single-photon ionization upon absorption of a photon with energy $\omega_{02} + \delta\omega_1$ (high frequency component), which would promote the photoelectron exactly at 6.5 eV. The required photon energy $\omega_{02} + \delta\omega_1$ is available within the spectral width of the high frequency component ω_2 . Alternatively, the photoelectron can also be promoted from the LUMO exactly at 6.5 eV upon absorption of a photon with energy $\omega_{40} - \delta\omega$ (high frequency component) where the required photon energy $\omega_{40} - \delta\omega$ is again available within the spectral width of ω_4 . Another option for the photoelectron to acquire a kinetic energy of 6.5 eV from the LUMO is to absorb a photon with energy $\omega_{50} - \delta'$ (high frequency component) where again the required photon energy is available within the spectral width of the high frequency components of the pulse. These three possibilities defines the first scenario, \mathcal{S}_1 , and involves resonant excitation of the LUMO upon absorption of a photon energy within the spectral width the low energy component ω_1 followed by single-photon ionization mediated by the high frequency components of the field. The respective two-photon ionization scheme is highlighted in red in Fig. 2(f) in the manuscript. Implicitly, the scenario \mathcal{S}_1 as discussed above may be viewed a pump-probe scheme where the low frequency components (pump) arrives earlier in time to first excite the LUMO, followed by ionization mediated by the high frequency components (probe-pulse) arriving latter in time.

It is worth noticing, however, that exchanging the temporal order of the pump and probe pulses discussed above also lead to a resonantly enhanced two-photon ionization scheme that allows the different contributing two-photon pathways to interfere exactly at 6.5 eV. Such a scenario, consisting in high (pump) and low (probe) frequency components arriving earlier and latter in time,

¹ also found in Eq. (8) in the manuscript

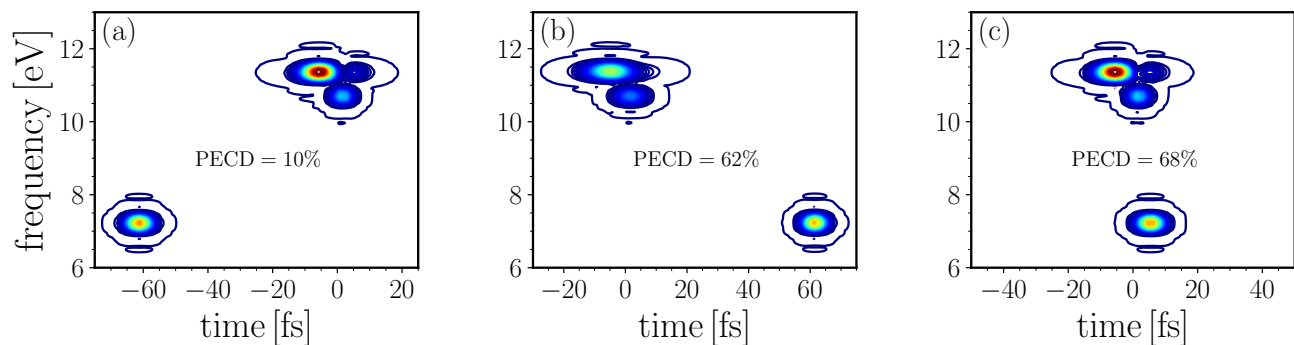


FIG. 5. Time-frequency distribution of the fully-optimized pulse for three different time delays between its low and high frequency components. Pump-probe scheme corresponding to the scenario \mathcal{S}_1 is shown in (a). In this scenario, the pump and probe pulses, carrying the low and high frequency components, respectively, are temporally separated. Only the two-photon pathway probing the LUMO participates in the photoionization process. Control scheme corresponding to the scenario \mathcal{S}_2 is shown in (b). Pump and probe pulses carrying high (pump) and low (probe) frequency components are temporally separated. Maximum achievable PECD amounts to 62% and the corresponding PECD contains the signature of all orbitals, except the LUMO. Optimal scheme corresponding to the scenario \mathcal{S}_3 , whereby pump and probe pulses carrying low and high frequency components overlaps in time is shown in (c). This scenario maximizes the PECD by exploiting interference of all two-photon pathways including that through the LUMO.

respectively, is referred to as \mathcal{S}_2 , and the corresponding two-photon ionization scheme is highlighted in blue in Fig. 2(f) in the manuscript. In detail, absorption of a photon with energy ω_{20} (high frequency component) resonantly populates the LUMO+1. The photoelectron can *then* be promoted at 6.5 eV upon absorption of a photon with energy $\omega_{10} + \delta\omega_1$ which is available within the spectral width of ω_1 (low frequency component). Alternatively, according to the field spectrum in Fig. 3(c), also the LUMO + 3 can be excited through the high frequency component ω_{30} contained in the field, and the photoelectron can *latter* be promoted at 6.5 eV upon absorption of $\omega_{10} - \delta\omega$, available within the spectral width of ω_1 . Finally, same two-photon mechanism can be retrieved by resonantly exciting the LUMO + 4.

The main difference between the scenarios \mathcal{S}_1 and \mathcal{S}_2 lies in the different orbitals that are excited in the sequential excitation-ionization scheme. In \mathcal{S}_1 , only the LUMO is excited by the pump pulse and ionized afterwards. The PECD thus contains the signature of the LUMO alone.

Conversely, in \mathcal{S}_2 , all orbitals except the LUMO are excited by the pump pulse containing the high frequency components. Thus, after ionization, the PECD contains the signature of all orbitals, except that of the LUMO.

Finally, the third possible scenario, \mathcal{S}_3 , consists in both low and high frequency components of the optimized spectrum sharing a given time window, this is, pump and probe pulses overlapping in time. The main interest in overlapping pump and probe pulses lies in the fact that, in contrast to \mathcal{S}_2 , also the LUMO can be excited by the pulse that now contains not only high-frequency components to excite the LUMO + j orbitals, for $j \geq 1$, but also the required low frequency components to excite the LUMO. Consequently, the signature of the LUMO along with higher-lying orbitals is imprinted in the PECD. It remains to be seen, however, which scenario, namely \mathcal{S}_1 ,

\mathcal{S}_2 or \mathcal{S}_3 indeed corresponds to the optimized two-photon scheme leading to a PECD of 68% at 6.5 eV.

In order to disentangle the optimal scenario from all three possible cases discussed above, we have introduced a time delay, τ , between the low and high frequency components, which will be varied from negative to positive values. Positive (negative) delays correspond to the high-frequency components arriving before (after) the low-frequency components. Analyzing the PECD as a function of τ as presented in Fig. 3(c) in the manuscript allow us to retrieve the optimal scenario. In fact, a time-frequency analysis of the optimized pulse for the optimal time-delay yielding to 68%, tells us about whether the low and high frequency components overlap in time (\mathcal{S}_3) or whether they are temporally separated, i.e. sequential pump-probe scheme (\mathcal{S}_2 or \mathcal{S}_3)². Also note that since both low and frequency components are spectrally separated (not overlapping), the power spectrum remains unaltered.

In Fig. 3(c) in the manuscript, we show the PECD as a function of the time-delay τ . The section highlighted in red in Fig. 3(c) corresponds to the first scenario \mathcal{S}_1 . Figure 5(a) shows the Wigner distribution function for a time-delay corresponding to \mathcal{S}_1 . As discussed before, only the LUMO participate in the sequential two-photon ionization process, as the low frequency components arrive earlier in time. This is also confirmed by Fig. 3(c) (highlighted in red) in the manuscript. In fact, the corresponding PECD exhibits no oscillation as a function

² Although there is no need to introduce an external delay τ to evaluate the Wigner distribution function of the fully-optimized pulse, i.e. the optimized pulse already contains the optimal time-delay, this procedure allows us to confirm the role of the pump and probe pulses in terms of the orbitals being excited prior to the ionization step.

of the time-delay, which is explained by the absence of interfering two-photon ionization pathways at 6.5 eV, as only the LUMO contributes to the PECD. The steady value for the PECD amounts to 10%.

For positive time delays (highlighted in blue in Fig. 3(c) in the main text) the pump and probe pulses are now switched. This is, the high frequency components arrive earlier in time, as verified by the Wigner distribution function shown in Fig. 5(b), which shows the time-frequency distribution for a time delay corresponding to \mathcal{S}_2 . In this scenario, the pump pulse – now containing the high-frequency components of the spectrum – creates a wavepacket defined by a superposition of all orbitals except the LUMO, which evolves under the field-free Hamiltonian. After a time delay τ , the probe pulse containing the low frequency components ionizes the prepared wavepacket that has gained a given time delay-dependent phase. The signature of the interference among the contributing two-photon pathways can be seen in Fig. 3(c) (highlighted in blue) in the manuscript. The corresponding PECD exhibits an oscillatory behavior as a function of the time-delay, associated with the time delay-dependent phase accumulated by the prepared wavepacket during the time-delay between the pump and probe pulses. According to Fig. 3(c) in the manuscript, the maximum PECD for this sequential pump-probe scheme accounts for 55%³, which is not 68% found for the fully optimized pulse. This means the optimal scheme does not correspond to a pump-probe scheme whereby low and high and frequency components are temporally separated.

Only for a specific time delay of 8.2 fs, the optimal PECD (68%) is retrieved, cf. Fig. 3(c) (highlighted in yellow) in the manuscript. The corresponding time-frequency distribution is depicted in Fig. 5(c). It shows that the optimal case corresponds to both “pump” and “probe” pulses sharing a particular temporal window. In other words, the optimal scenario correspond to low and high frequency components overlapping in time, i.e. \mathcal{S}_3 . The stronger PECD of 68% compared to that obtained in the framework of \mathcal{S}_2 (55%) can be explained by exploiting interference of all the pathways, including the two-photon ionization through the LUMO⁴, which now also contribute to the PECD. The respective ionization scheme is depicted in Fig. 2(f) (highlighted in yellow) in the manuscript.

As alluded to above, we conclude that the highly efficient control of PECD is achieved via various $(1+1')$ REMPI pathways that probes different intermediate states to constructively interfere at a common photoelectron energy. By introducing a time delay between the low and high frequency components of the optimized

field, we have shown that the control mechanism based on multiple even-parity interference pathways presented in this work outperforms the standard sequential pump-probe scheme as it maximizes the number of molecular states that constructively contribute to the dichroism at an optimal photoelectron kinetic energy.

VII. MAXIMIZING THE PECD AT A SPECIFIC PHOTOELECTRON ENERGY USING THE MULTIPLE $(1' + 1)$ -REMPI SCHEME

As a complement to the PECD study with a peak of the photoelectron distribution at an energy of 6.5 eV discussed in the main text, we provide here the optimization results for a peak at 10 eV. The latter corresponds to the photoelectron energy for which the largest PECD, of about 20%, is obtained when using a bichromatic $(\omega, 2\omega)$ pulse. Starting from a reference field driving one-photon ionization only, Fig. 6(a) displays the corresponding single-photon PECD, with a maximum of 8.5% at a photoelectron kinetic energy ϵ_k^* of 10 eV. The one-photon ionization scheme is schematized in Fig. 6(d). Note that the PECD value can also be retrieved from Figure 1(b) in the main text (“one-photon” regime) at a photon energy of $\omega = 21.88$ eV (solid-blue lines).

The PECD resulting from the optimized bichromatic $(\omega, 2\omega)$ field is shown in Fig. 6(b). In this case, the second harmonic and fundamental photon energies correspond to $\omega = 21.88$ eV and $\omega/2 = 10.94$ eV, respectively. The orbital energies for the LUMO and LUMO + 1 are equal to -4.80 and -0.97 eV, respectively. In contrast to the case of a photoelectron energy $\epsilon_k^* = 6.5$ eV discussed in the main text, where the excitation due to absorption of a photon with energy corresponding to the fundamental was found to exactly lie in between the orbital energies of the LUMO and LUMO + 1 (at -2.69 eV), cf. main text, here, $\omega_0 + \omega/2 = -0.93$ eV, to be compared to the energy of the LUMO + 1, i.e., $\omega_0 + \omega_{20} = -0.97$ eV. Consequently, for an optimal photoelectron energy $\epsilon_k^* = 10$ eV, the efficiency of the two-photon ionization is enhanced compared to that at 6.5 eV discussed in the main text. As a result, a larger magnitude for the PECD is found (20% instead of 14%). The corresponding ionization scheme is depicted in Fig. 6(e).

Finally, the PECD resulting from the multiple two-photon ionization scheme converging at 10 eV is shown in Fig. 6(c). A maximum PECD = 64% exactly at 10 eV is obtained. Analogously to the enhancement mechanism at 6.5 eV discussed in the main text, the physical mechanism responsible for a PECD of 64% at 10 eV is also based on multiple $(1' + 1)$ -REMPI process probing different molecular orbitals and coherently converging at the same final photoelectron energy. Only two-photon processes participate⁵, with no contribution from

³ further optimization within this pump-probe scheme leads to a PECD of 62%, as discussed in the manuscript.

⁴ since the low frequency is now also available at the same time that the higher frequency components

⁵ main contribution arising from the first four LUMO orbitals. The

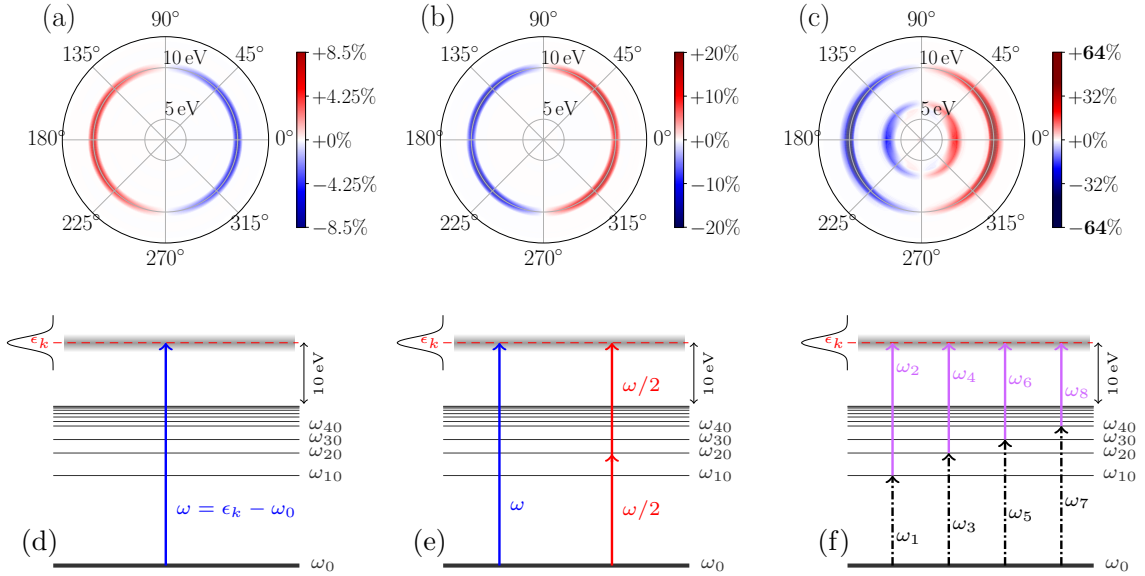


FIG. 6. PECD obtained with a reference field driving one-photon ionization only (a), optimized bichromatic ($\omega, 2\omega$) pulse (b), and making use of interference in even-parity two-photon pathways (c). For all three schemes, the corresponding maximum PECD is obtained at the same final photoelectron kinetic energy ϵ_k^* of 10 eV. Ionization and control schemes for the guess and optimized ($\omega, 2\omega$) pulses are shown in panels (d) and (e), respectively. The control mechanism for even-parity pathway interference (f) is based on probing different intermediate states that interfere constructively at a common continuum photoelectron energy within the spectral bandwidth.

one-photon ionization and interference between opposite-parity ionization pathways at 10 eV. The corresponding ionization scheme is as depicted in Fig. 6(f).

For the optimization based on the multiple ($1' + 1$)-REMPI (coherently) converging at 10 eV, the photon energies $\omega_j = \omega_{j0}$ together with $\omega_{j+n} = \epsilon_k^* - \omega_{j,0} + |\omega_0|$, for $j = 1, n$ were kept fixed, whereas the remaining control variables, cf. Eq. (9) in the manuscript, were optimized. Here, n refers to the number of two-photon pathways, each one probing n different orbitals, to be accounted for. Figure 6(f) thus schematizes the (multiple) two-photon ionization scheme for $n = 4$, i.e. probing $n = 4$ different intermediate states but converging at the same photoelectron energy, within the spectral width.

Reducing the number n of contributing two-photon pathways results in a decrease of PECD (abs. value) at its maximum peak distribution. Figure 7 shows the optimized PECD at 10 eV obtained with $n = 1$ (panels a-d) and $n = 2$ (panels c, f) distinct two-photon ionization pathways. For Fig. 7(a), the pulse is parametrized according to Eq. (9) in the main text with only two frequencies components: the frequencies ω_1 and ω_2 , as indicated in Fig. 7(d), are kept fixed and the remaining pulse parameters are optimized. Analogously, for Fig. 7(b), the

optimized field consists in a pulse with two (fixed) frequencies components ω_3 and ω_4 , as indicated in Fig. 7(e), and the remaining pulse parameters are treated as optimization variables. Finally, for Fig. 7(c), i.e. $n = 2$, the optimized pulse consist of four (fixed) frequencies, namely $\omega_1, \omega_2, \omega_3, \omega_4$, as indicated in Fig. 7(f). In all three scenarios the optimizations were performed independently.

The maximum chiral response is obtained at the same final photoelectron energy for all three cases. However, from Fig. 7(a) and (b), it is apparent that both two-photon ionization pathways imprint their own signature to the PECD, as the resulting magnitude of PECD changes dramatically depending on the two-photon pathway. Consequently, the contributing two-photon pathway plays a critical role for maximizing the PECD. Specifically, for a two-photon pathway probing only the LUMO orbital followed by ionization, cf. Fig. 7(d), the PECD amounts to 4.4% only. In contrast, the ionization pathway probing the LUMO + 1 with subsequent ionization, cf. Fig. 7(e), results in an orientation averaged PECD of 47%. When the optimization is performed using the combined two-photon pathways, cf. Fig. 7(f), the PECD is enhanced, in a synergetic manner, to 58%, as shown in Fig. 7(c), indicating the coherent nature of the interference process. Furthermore, adding two more pathways, such that also the LUMO + 2 and LUMO + 3 are probed, as indicated in Fig. 6(f), results in the optimal scheme for a photoelectron energy ϵ_k^* of 10 eV, with PECD equal to 64%, as shown in Fig. 6(c). The optimal

transition dipole moments from the HOMO to these orbitals depends on the molecular orientation with respect to the electric field polarization direction. The square of the isotropically averaged transition dipole moments (atomic units) correspond to 0.28, 0.16, 0.20 and 0.02, respectively.

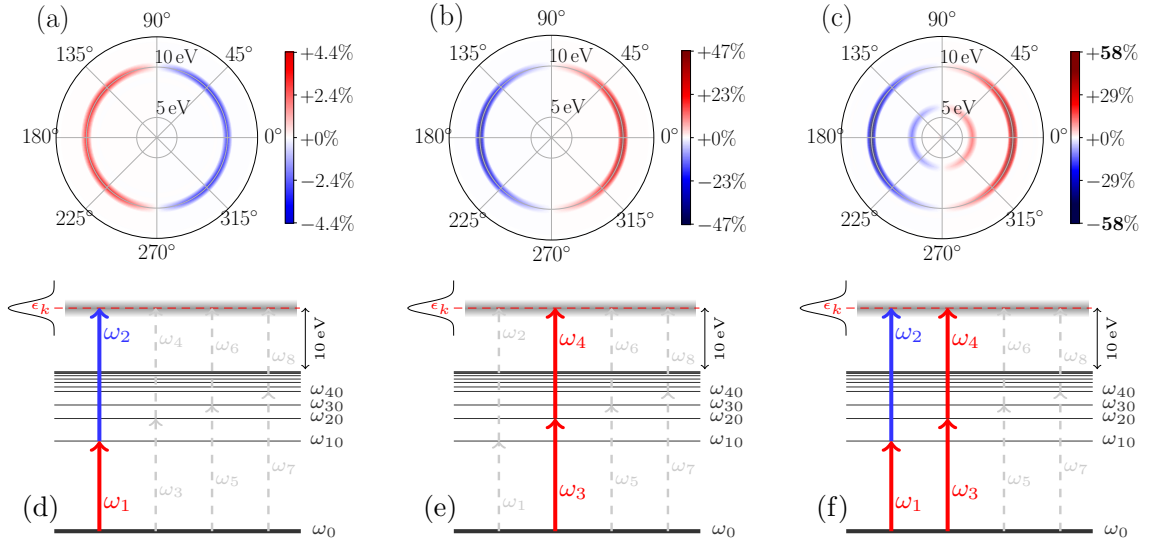


FIG. 7. Optimized anisotropic response obtained within the multiple $(1' + 1)$ -REMPI scheme using one, panels (a) and (b) and two (c) distinct two-photoionization pathways. In panel (a), the REMPI process consist in resonant excitation of the LUMO orbital, followed by ionization out of the resonantly excited state, as schematized in panel (d). The resulting optimized PECD corresponds to 4.4%. Excitation of the LUMO + 1 instead of the LUMO (e) in the REMPI process results in a significant larger PECD effect (47%), at the same photoelectron kinetic energy (10 eV). Combination of both schemes, i.e., of the two photoionization pathways, enhances the PECD to (58%) (c). In all three cases, the optimization were carried independently. Incorporation of additional pathways increases the PECD effect even more, e.g. PECD = 64% for four two-photoionization pathways converging at the same photoelectron energy as displayed in Fig. 6(c) and Fig. 6(f).

multiple $(1' + 1)$ REMPI scheme, for 10 eV, therefore consists in four different two-photon ionization pathways, i.e. $n = 4$, converging and constructively interfering at the same photoelectron energy, as depicted in Fig. 6(f).

Finally, Fig. 8 presents a photon energy vs. relative phase correlation map for the PECD obtained with a bichromatic $(\omega, 2\omega)$ pulse with fixed FWHM and intensities, corresponding to that of the optimized bichromatic $(\omega, 2\omega)$ field sketched in Fig. 6(e). The total PECD and anisotropy parameters defined in Eq. (59) for the first and second order process –and their interference– are shown in Fig. 8, panels (a)-(d), respectively, as a function of the photon energy (fundamental) and relative phase between the fundamental and second harmonic. The PECD in Fig. 8(a) corresponds to the maximum PECD (abs. value) extracted from the PECD distribution in Eq. (59), obtained at the particular photoelectron kinetic energy ϵ_k^* and direction $\theta_{k'}^*$, at which the PECD is maximal, i.e., $|\text{PECD}(\epsilon_k^*, \theta_{k'}^*, \pi/2)| \geq |\text{PECD}(\epsilon_k, \theta_{k'}, \pi/2)|, \forall (\epsilon_k, \theta_{k'})$.

It is worth noting, however, that interpretation of Fig. 8(a) must be taken with precaution since a large magnitude of PECD obtained with a bichromatic $(\omega, 2\omega)$ field does not necessarily mean that interference between one-photon and two-photon pathways plays a significant role. In fact, from Figs. 8(a) and (c), it is apparent that the large magnitude of positive PECD, of $\approx 38\%$, is almost exclusively due to two-photon ionization pathways. This finding is further confirmed by removing the second harmonic from the bichromatic field. Note also that this

large value can already be retrieved from the red curve in Figure 1(b) of the main text, corresponding to the two-photon regime.

Conversely, in the lower part of Fig. 8(a), the large negative PECD, of $\approx -27\%$, is mainly due to a one-photon process, which can be seen by comparing panels (a) and (b) in Fig. 8. Very importantly, the angle at which the PECD is maximal, $\theta_{k'}^*$, must, of course, also be taken into account. In fact, although the interference term, $\beta_{2,1}^{int}(\epsilon_k^*)$, shown in Fig 8(d) does not vanish for the pulse parameters yielding a PECD equal to -27% , a further inspection of the direction $\theta_{k'}^*$ of photoelectron emission at which the PECD is -27% reveals that $\theta_{k'}^*$ corresponds to 0 (and π). For $\theta_{k'}$ equal to 0 (nor π), the interference term between opposite-parity photoionization pathways cannot contribute at all, cf. Eq (59). The same applies for the maximum PECD of $+38\%$, previously discussed.

Instead, the maximum contribution from the interference term, or more rigorously speaking, the best compromise between all terms in Eq. (59) to maximize the PECD while requiring the interference term to play a non-negligible role is found for $\omega/2 = 10.9$ eV (fundamental) for a total PECD of 20% at a photoelectron kinetic energy distribution of 10 eV., cf. Fig. 8 (a) and (d), with an angle $\theta_{k'}^*$ equal to $\pi/4$ (modulo π), cf. Fig. 6(b).

-
- [1] L. Brillouin, *La méthode du champ self-consistent* (Hermann, 1933).
- [2] A. Szabo and N. S. Ostlund, *Modern quantum chemistry: Introduction to advanced electronic structure theory* (Courier Corporation, 2012).
- [3] M. Baertschy, T. N. Rescigno, and C. W. McCurdy, *Phys. Rev. A* **64**, 022709 (2001).
- [4] W. H. Miller and B. M. D. D. Jansen op de Haar, *J. Chem. Phys.* **86**, 6213 (1987).
- [5] F. A. Gianturco, R. R. Lucchese, and N. Sanna, *J. Chem. Phys.* **100**, 6464 (1994).
- [6] A. P. P. Natalense and R. R. Lucchese, *J. Chem. Phys.* **111**, 5344 (1999).
- [7] L. Greenman, R. R. Lucchese, and C. W. McCurdy, *Phys. Rev. A* **96**, 052706 (2017).
- [8] N. Rohringer, A. Gordon, and R. Santra, *Phys. Rev. A* **74**, 043420 (2006).
- [9] A. R. Edmonds, *Angular momentum in quantum mechanics* (Princeton University Press, 2016).
- [10] R. E. Goetz, M. Merkel, A. Karamatskou, R. Santra, and C. P. Koch, *Phys. Rev. A* **94**, 023420 (2016).
- [11] H.-J. Werner, P. J. Knowles, G. Knizia, F. R. Manby, M. Schütz, P. Celani, T. Korona, R. Lindh, A. Mitrushenkov, G. Rauhut, K. R. Shamasundar, T. B. Adler, R. D. Amos, A. Bernhardsson, A. Berning, D. L. Cooper, M. J. O. Deegan, A. J. Dobbyn, F. Eckert, E. Goll, C. H. I, A. Hesselmann, G. Hetzer, T. Hrenar, G. Jansen, C. Köppl, Y. Liu, A. W. Lloyd, R. A. Mata, A. J. May, S. J. McNicholas, W. Meyer, M. E. Mura, A. Nicklass, D. P. O’Neill, P. Palmieri, D. Peng, K. Pflüger, R. Pitzer, M. Reiher, T. Shiozaki, H. Stoll, A. J. Stone, R. Tarroni, T. Thorsteinsson, and M. Wang, “Molpro, version 2012.1, a package of ab initio programs,” .
- [12] H.-J. Werner, P. J. Knowles, G. Knizia, F. R. Manby, and M. Schtz, *Wiley Interdisciplinary Reviews: Computational Molecular Science* **2**, 242 (2012).